



# Lyapunov-based control and trajectory tracking of a 6-DOF flapping wing micro aerial vehicle

Bishoy E. Wissa · Karim O. Elshafei ·  
Ayman A. El-Badawy 

Received: 7 August 2019 / Accepted: 11 January 2020  
© Springer Nature B.V. 2020

**Abstract** In this work, a high-fidelity nonlinear and time-periodic six degrees-of-freedom dynamic model of a flapping wing micro aerial vehicle has been developed. The model utilized Lagrange's equations for quasi-coordinates. A quasi-steady aerodynamic model that includes the effect of leading-edge vortex and rotational circulation was implemented. Averaging technique was used to obtain a time-invariant dynamic model for the purpose of designing a trajectory tracking control law. The sensitivity of aerodynamic forces and moments to the control parameters, namely: flapping frequency, flapping bias and stroke plane angles, was determined exploiting control derivatives. The developed controller has two loops. The outer-loop, employing integral sliding mode controller, generates desired cycle-averaged aerodynamic forces and moments. The inner loop employs a novel control allocation method. The proposed inner-loop controller provides a closed-loop feedback solution that ensures that the chosen control parameters provide the desired aerodynamic forces and moments. Simulation studies indicate that the proposed controller applied on the high-fidelity

six degrees-of-freedom dynamic model successfully achieves trajectory tracking.

**Keywords** Flapping wing micro aerial vehicle · Leading-edge vortex · Rotational circulation · Averaging · Control allocation method · Integral sliding mode control

## 1 Introduction

The amazing steady flight capabilities of biological insects and birds inspired researchers to go deep into the topic of flapping wing micro aerial vehicles (FWMAVs). Flapping wing flight can be used in many applications such as: surveillance, reconnaissance and mapping. To accomplish these applications, high-fidelity dynamic and aerodynamic models for the FWMAV were developed. Different control strategies are designed in the literature to achieve trajectory control for this complex system. Some of these strategies will be discussed in this section.

Zhang et al. [25] simulated the bumblebee model in a biology-inspired dynamic flight simulator. The simulated model includes: kinematics, unsteady aerodynamics and dynamics of the insect flight. They addressed controlling the three axis attitudes (roll, pitch and yaw) of the linear-averaged six degrees-of-freedom (DOF) hovering model using proportional-derivative (PD) controller. During hovering, The controller suc-

---

B. E. Wissa · K. O. Elshafei · A. A. El-Badawy (✉)  
Mechatronics Engineering Department, Faculty of  
Engineering and Materials Science, German University in  
Cairo, Cairo, Egypt  
e-mail: ayman.elbadawy@guc.edu.eg

B. E. Wissa  
e-mail: bishoy.emil@guc.edu.eg

K. O. Elshafei  
e-mail: karim.elshafei@guc.edu.eg

ceeded in stabilizing the attitude of the model in the presence of limited disturbance.

Lee et al. [15] developed a nonlinear time-varying three-DOF longitudinal model for the FWMAV. The aerodynamic model employed is a quasi-steady model which accounts for the translational and rotational aerodynamics. They designed a full-state feedback stabilization controller based on a linear time-invariant (LTI) model. The proposed controller succeeded in controlling and stabilizing the linear and the high-fidelity three-DOF models.

Doman et al. [9] proposed a six-DOF model that does not account for wing inertia effects. The model used split-cycle constant-period frequency modulation for varying the flapping speed of up and down-strokes. They also added a bob-weight to provide control authority over five-DOF. Aerodynamic loads were derived based on blade element theory and experimental unsteady aerodynamic model. A pseudo-inverse control allocation scheme was used. Moreover, a linear PD controller is implemented to achieve waypoint tracking.

Oppenheimer et al. [20] controlled six-DOF FWMAV using quarter-cycle constant-period frequency modulation. The used aerodynamic model is based on the blade element theory. This model did not cover the rotational, leading-edge vortex (LEV), interactions between the wings or wake capture effects. The control allocation method and the controller proposed are done similar to [9]. They simulated the controller using the periodic aerodynamic forces and moments. The controller showed acceptable performance.

All the previous discussed controllers are concerned with linear controllers. However, nonlinear controllers enhance controlling the FWMAV [22].

Bluman et al. [4] controlled a bumblebee inspired model to hover in the pitch plane, using two different sliding mode control (SMC) approaches: the classical and the second-order SMC. The wing's control parameters were calculated using the Moore–Penrose pseudo-inverse method. The results showed that the classical SMC outperforms the second-order SMC. It is shown that the body frame velocity in the  $z$ -axis is brought to zero in around 25 flapping cycles with classical SMC, compared to around 40 flapping cycles using second-order SMC.

Chirattananon et al. [5,6] proposed an adaptive SMC technique to control the lateral, altitude and attitude of a robotic insect. The inertia of the wings

was neglected, due to their small values. The model accounts only for stroke averaged dynamics. Whereas, the aerodynamic forces and moments are modeled by the blade element method. The thrust and torques are suggested to be linear-averaged functions. The simulation results showed the ability of the controller to accomplish millimeter-scale precision for simple lateral maneuvers, vertical takeoff, and landing flights.

Banazadeh et al. [1] designed a control law based on the averaged model of the six-DOF humming bird using adaptive SMC. The considered model neglects the mass and inertia of the wings. The derived aerodynamic model is based on quasi-steady assumptions. Two feedforward artificial neural networks were used as a control allocation method. In spite of having model uncertainties and presence of input disturbances, the designed controller succeeded in stabilizing the proposed model.

Kalliny et al. [14] derived an accurate nonlinear time-variant longitudinal model of FWMAV including the mass and inertia of the wings. The aerodynamic model presented accounts for rotational circulation and LEV. A command-filtered integral backstepping controller is proposed for longitudinal trajectory tracking. The controller is derived based on the averaged model. However, the results showed good tracking performance in simulations carried out on the high-fidelity model.

Accordingly, most of the derived dynamic models neglect the mass and the inertia of the wings. While others neglect the aerodynamic rotational circulation effect which is essential to avoid pitch dynamics instability [1]. Hence, developing a six-DOF model including the aforementioned considerations would be necessary for the sake of precise control system simulation.

In addition, some of the work used linear control techniques and others used nonlinear control approaches to control the FWMAV. Besides, part of the work used iterative techniques as a control allocation method which are not preferred for their large computational complexity. While others used open-loop mathematical techniques as control allocation method which are commonly performed on linearized aerodynamic loads. However, these approaches provide solutions in the vicinity of the linearization points.

Compared to previous studies in the literature, the current work proposes a high-fidelity six-DOF dynamic model of the FWMAV based on Lagrange's equations for quasi-coordinates [16]. Aerodynamic modeling is

adopted from a quasi-steady model proposed by Dickinson et al. [7] which accounts for LEV and rotational circulation effects. The averaging theory is applied to obtain cycle-averaged aerodynamic loads suited for controller design. The control law employs two nested control loops. The outer control loop includes an integral sliding mode control (ISMC) law that manipulates the FWMAV dynamics. The ISMC provides robust performance against model uncertainties and external disturbances. While the inner control loop includes a proposed Lyapunov-based control allocation method. The proposed method is a closed-loop control law which provides accurate continuous solutions.

In order to validate the proposed controller along with the control allocation method, simulations are carried out on three different models. The averaged model which accounts for averaged aerodynamic loads only, the periodic model which accounts for periodic time varying aerodynamic loads, and the high-fidelity model which accounts for periodic aerodynamic loads while including wing mass and inertia effects. The proposed controller shows robust performance against parametric uncertainties and external disturbances in achieving precise trajectory tracking with feasible control inputs in the three different simulations.

The main contributions in the current work are summarized in the following points

- High-fidelity six-DOF FMWAV dynamic model that accounts for wing mass and inertia effects is presented.
- An aerodynamic model that accounts for LEV and rotational circulation effects is adopted.
- A novel Lyapunov-based closed-loop control allocation method is proposed. Precise trajectory tracking control for a six-DOF FWMAV high-fidelity model using ISMC is achieved.

The rest of the paper is organized as follows: Sect. 2 presents dynamic and aerodynamic modeling of the FWMAV. Development of a control oriented model is derived in Sect. 3. Section 4 demonstrates the outer and inner loop controller design. Simulation results are presented in Sect. 5. Finally, conclusions and directions for future work are in Sect. 6.

## 2 Dynamic model

The FWMAV model addressed here is similar to the one addressed in [14], while also including a left and right

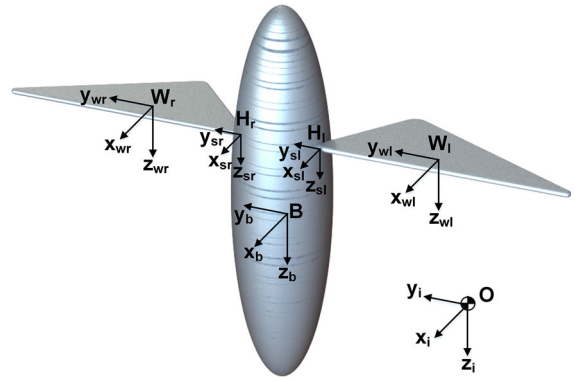


**Fig. 1** Model frames

stroke frames as shown in Fig. 1. The model consists mainly of three rigid bodies: the body, the left and right wings.

Several frames of reference are defined for FWMAV, as shown in Fig. 1. First, the inertial frame ( $i$ ) which is a fixed frame, whose origin is point  $O$  fixed to the reference ground. Second, the body frame ( $b$ ), whose origin is the body center of mass  $B$  [14]. Third, two stroke frames are defined for the stroke planes, where the flapping of each wing takes place. Right stroke frame ( $sr$ ) and left stroke frame ( $sl$ ) whose centers are the points of hinge center of mass,  $H_r$  and  $H_l$ , respectively. Finally, two wing frames are attached to the wings: the right wing frame ( $wr$ ) and the left wing frame ( $wl$ ), each centered at the respective wing center of mass,  $W_r$  and  $W_l$ .

Position, velocity and angular velocity vectors will be denoted according to the following notation:  $\{^f V_a^b\}$  where ( $V$ ) is the position, velocity or angular velocity vector of point or frame ( $a$ ), with respect to point or frame ( $b$ ), expressed in frame ( $f$ ).

### 2.1 Body kinematics

The motion of the vehicle is presented in the inertial frame ( $i$ ) using the following vectors: position vector of the body center of mass ( $B$ ) with respect to the origin of the fixed frame ( $O$ ) is given by

$$\{^i r_B^O\} = \{x, y, z\}^T \quad (1)$$

where  $x$ ,  $y$  and  $z$  are the distance from the origin ( $O$ ) to the body center of mass ( $B$ ) in the  $x$ ,  $y$  and  $z$  inertial axes, respectively. While  $T$  represents the transpose operator.

Euler angles defining the orientation of the body with respect to the inertial axes are expressed as

$$\{\phi_b^i\} = \{\Phi, \Theta, \Psi\}^T \quad (2)$$

where  $\Phi$ ,  $\Theta$  and  $\Psi$  are the roll, pitch, and yaw orientations, respectively.

Linear velocity of the body center of mass ( $B$ ) with respect to the origin of the fixed frame ( $O$ ) is defined as

$$\{^b v_B^O\} = \{u, v, w\}^T \quad (3)$$

where  $u$ ,  $v$  and  $w$  represent the velocity of the body center of mass ( $O$ ) in the  $x$ -,  $y$ - and  $z$ - body axes, respectively.

Angular velocity of body frame ( $b$ ) with respect to inertial frame ( $i$ ) expressed as

$$\{^b \omega_b^i\} = \{p, q, r\}^T \quad (4)$$

where  $p$ ,  $q$  and  $r$  are the angular velocities around the  $x$ ,  $y$  and  $z$  body axes, respectively.

The rate of change of the position vector in the inertial frame is defined in terms of the velocity vector in the body frame as

$$\{^i \dot{r}_B^O\} = [R_b^i] \{^b v_B^O\} \quad (5)$$

where the rotation matrix  $R_b^i$  is given by

$$[R_b^i] = \begin{bmatrix} C_\Theta C_\Psi & C_\Theta S_\Psi & -S_\Theta \\ S_\Phi S_\Theta C_\Psi - C_\Phi S_\Psi & S_\Phi S_\Theta S_\Psi + C_\Phi C_\Psi & S_\Phi C_\Theta \\ C_\Phi S_\Theta C_\Psi + S_\Phi S_\Psi & C_\Phi S_\Theta S_\Psi - S_\Phi C_\Psi & C_\Phi C_\Theta \end{bmatrix}^T \quad (6)$$

where  $C_x$  corresponds to  $\cos(x)$  and  $S_x$  corresponds to  $\sin(x)$ .

In addition, the rate of change of the Euler angles are defined in terms of the angular velocity in the body frame as

$$\{^i \dot{\phi}_b^i\} = [E_b^i]^{-1} \{^b \omega_b^i\} \quad (7)$$

where  $[E_b^i]$  is defined as

$$[E_b^i] = \begin{bmatrix} 1 & 0 & -S_\Theta \\ 0 & C_\Phi & C_\Theta S_\Phi \\ 0 & -S_\Phi & C_\Theta C_\Phi \end{bmatrix} \quad (8)$$

## 2.2 Wing kinematics

In this work, only flapping and feathering wing rotations are considered. Flapping angle  $\kappa(t)$  is the wing

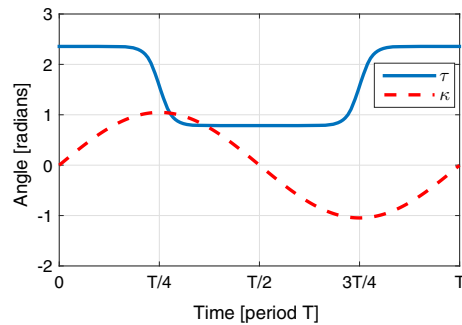


**Fig. 2** Feathering and flapping angles for one complete cycle

rotation about the  $z_s$  axis, while feathering angle  $\tau(t)$  is the wing rotation about  $y_w$  axis as shown in Fig. 3. A harmonic flapping angle  $\kappa(t)$  is defined as [14]

$$\kappa(t) = A_\kappa \sin(\omega_o t + \zeta(t)) + \beta(t) \quad (9)$$

where  $A_\kappa$  is the flapping amplitude,  $\omega_o$  is the nominal flapping frequency,  $\zeta(t)$  is the phase shift and  $\beta(t)$  is the flapping bias.  $\kappa(t)$  is shown in Fig. 2 for  $\beta(t) = 0$ . The rate of change is defined as

$$\dot{\kappa}(t) = A_\kappa \omega_o (1 + \delta(t)) \cos(\omega_o t + \phi(t)) + \dot{\beta}(t) \quad (10)$$

where  $\delta(t) = \dot{\phi}(t)/\omega_o$  which is defined as the variation of flapping frequency [21]. The feathering angle  $\tau(t)$ , which is shown in Fig. 2, will be considered as a square wave using a hyperbolic tangent function to avoid discontinuity (ensure differentiability) [3], represented as follows

$$\tau(t) = \frac{\pi}{2} + \frac{A_\tau}{\tanh C_\tau} \tanh[C_\tau \cos(\omega_o t + \phi(t))] \quad (11)$$

where in the downstroke a constant angle of  $(\pi/2 - A_\tau)$  is applied, and flips in the upstroke with a constant angle of  $(\pi/2 + A_\tau)$ .  $C_\tau$  is a constant that determines the sharpness of the square wave and is set to 5. In this model, asymmetric flapping is applied. Independent flapping and feathering parameters are expressed for each wing as follows:  $\kappa_l(t)$  and  $\tau_l(t)$  for the left wing,  $\kappa_r(t)$  and  $\tau_r(t)$  for the right wing. However, the flapping frequency ( $\omega_o$ ) is equal for both wings. For simplicity, the time dependency for  $\kappa(t)$  and  $\tau(t)$  will be dropped.

A rotation matrix between wing frame and stroke frame is given by

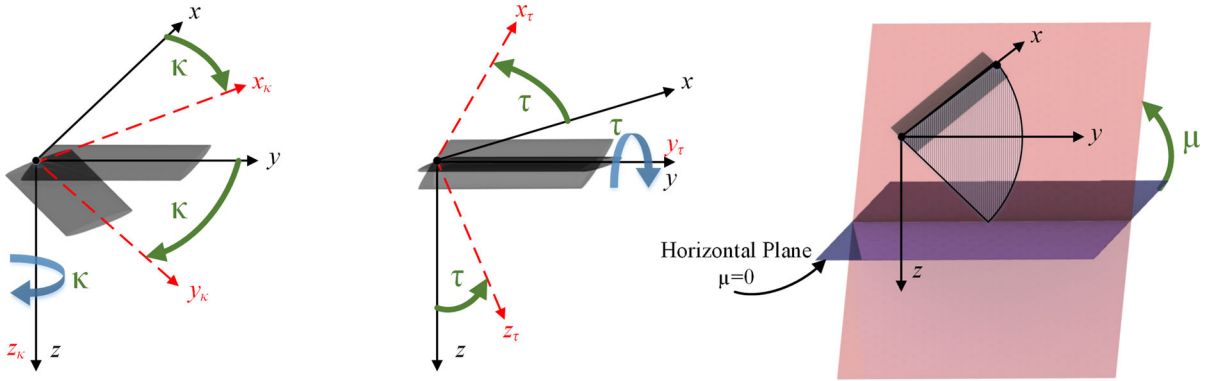


**Fig. 3** Wing's angles  $\kappa$ ,  $\tau$  and  $\mu$

$$[R_s^w] = \begin{bmatrix} \cos \tau \cos \kappa & \cos \tau \sin \kappa & -\sin \tau \\ -\sin \kappa & \cos \kappa & 0 \\ \sin \tau \cos \kappa & \sin \tau \sin \kappa & \cos \tau \end{bmatrix} \quad (12)$$

and between the stroke frame and the body frame,

$$[R_b^s] = \begin{bmatrix} \cos \mu & 0 & -\sin \mu \\ 0 & 1 & 0 \\ \sin \mu & 0 & \cos \mu \end{bmatrix} \quad (13)$$

where  $\mu$  is the stroke frame angle shown in Fig. 3.

Therefore, the rotation matrix from the wing frame to the body frame can be found as

$$[R_w^b] = [R_b^s]^T [R_s^w]^T \quad (14)$$

The angular velocity of the wing frame can be defined in the body frame as follows

$$\{^b \omega_w^b\} = \{^b \omega_s^b\} + \{^b \omega_w^s\} \quad (15)$$

where  $\{^b \omega_s^b\}$  is

$$\{^b \omega_s^b\} = \begin{bmatrix} 0 \\ \dot{\mu} \\ 0 \end{bmatrix} \quad (16)$$

while  $\{^s \omega_w^s\}$  is defined as

$$\{^s \omega_w^s\} = \begin{bmatrix} -\dot{\tau} \sin \kappa \\ \dot{\tau} \cos \kappa \\ \dot{\kappa} \end{bmatrix} \quad (17)$$

### 2.3 Kinetic energy

The kinetic energy of the system is presented as the sum of the energy produced due to the linear and angular velocities of the body and the two wings as follows

$$\bar{T}_{\text{sys}} = \bar{T}_B + \bar{T}_{W_r} + \bar{T}_{W_l} \quad (18)$$

where the kinetic energy of the body is defined as

$$\bar{T}_B = \frac{1}{2} m_B {}^b \mathbf{v}_B^O {}^b \mathbf{v}_B^O + \frac{1}{2} {}^b \omega_b^i {}^b \mathbf{I}_B^B {}^b \omega_b^i \quad (19)$$

and the kinetic energy of the wing is

$$\bar{T}_W = \frac{1}{2} m_W {}^b \mathbf{v}_W^O {}^b \mathbf{v}_W^O + \frac{1}{2} {}^b \omega_w^i {}^b \mathbf{I}_W^W {}^b \omega_w^i \quad (20)$$

where  $m_B$  and  $m_W$  are masses of the body and the wing, respectively. While  ${}^b \mathbf{I}_B^B$  is the body inertia tensor, expressed in the body frame as

$${}^b \mathbf{I}_B^B = \text{diag} \{I_{xxB}, I_{yyB}, I_{zzB}\} \quad (21)$$

while

$${}^w \mathbf{I}_W^W = \text{diag} \{I_{xxW}, I_{yyW}, I_{zzW}\} \quad (22)$$

is the wing inertia tensor expressed in the wing frame. It is expressed in the body frame as follows:

$${}^b \mathbf{I}_W^W = [R_w^b] {}^w \mathbf{I}_W^W [R_w^b]^T \quad (23)$$

Angular velocity of the wing with respect to the inertial frame is given by

$${}^b \omega_w^i = {}^b \omega_b^i + {}^b \omega_w^b \quad (24)$$

The velocity of the wing center of mass with respect to the inertial frame center is defined as

$${}^b \mathbf{v}_W^O = {}^b \mathbf{v}_B^O + {}^b \mathbf{v}_H^B + {}^b \mathbf{v}_W^H \quad (25)$$

where  ${}^b \mathbf{v}_H^B$  is the velocity of the hinge relative to the body center of mass,

$${}^b\mathbf{v}_H^B = {}^b\boldsymbol{\omega}_b^i \times {}^b\mathbf{r}_H^B \quad (26)$$

and  ${}^b\mathbf{v}_W^H$  is the velocity of the wing center of mass relative to the hinge center of mass, defined as

$${}^b\mathbf{v}_W^H = {}^b\boldsymbol{\omega}_w^i \times {}^b\mathbf{r}_W^H \quad (27)$$

Vectors  ${}^b\mathbf{v}_H^B$  and  ${}^b\mathbf{v}_W^H$  in Eqs. (26)–(27) represent first-order differential equations of the position vectors with respect to the time-parameter. These equations have an appropriate solution algorithm via coupled Riccati equations [11–13].

The position vectors for the right and left hinges and wings' center of masses are defined, respectively, as

$$\begin{aligned} {}^b\mathbf{r}_{H_l}^B &= \{0, -y_H, -z_H\}^T, & {}^b\mathbf{r}_{H_r}^B &= \{0, y_H, -z_H\}^T \\ {}^w\mathbf{r}_{W_l}^{H_l} &= \{0, -y_W, 0\}^T, & {}^w\mathbf{r}_{W_r}^{H_r} &= \{0, y_W, 0\}^T \end{aligned}$$

## 2.4 Lagrange's equations for quasi-coordinates

For the purpose of developing a six-DOF dynamic model for the FWMAV, Lagrange's equations for quasi-coordinates are used [16]. The kinetic energy of the system is represented in terms of the body linear and angular velocities, being the rates of the system quasi-coordinates yielding, the following

$$\frac{d}{dt} \left\{ \frac{\partial \mathbf{L}}{\partial [{}^b\mathbf{v}_B^O]} \right\} + [{}^b\tilde{\boldsymbol{\omega}}_b^i] \left\{ \frac{\partial \mathbf{L}}{\partial [{}^b\mathbf{v}_B^O]} \right\} - [\mathbf{R}_i^b] \left\{ \frac{\partial \mathbf{L}}{\partial [{}^i\mathbf{r}_B^O]} \right\} = \{ {}^b\mathbf{F}_B \} \quad (28)$$

$$\begin{aligned} \frac{d}{dt} \left\{ \frac{\partial \mathbf{L}}{\partial [{}^b\boldsymbol{\omega}_b^i]} \right\} + [{}^b\tilde{\mathbf{v}}_B^O] \left\{ \frac{\partial \mathbf{L}}{\partial [{}^b\mathbf{v}_B^O]} \right\} + [{}^b\tilde{\boldsymbol{\omega}}_b^i] \left\{ \frac{\partial \mathbf{L}}{\partial [{}^b\boldsymbol{\omega}_b^i]} \right\} \\ - [\mathbf{E}_i^b] \left\{ \frac{\partial \mathbf{L}}{\partial [\boldsymbol{\varphi}]} \right\} = \{ {}^b\mathbf{M}_B \} \end{aligned} \quad (29)$$

where  $\mathbf{L}$  is the Lagrangian term of the system given by the difference between kinetic and potential energy of the system, where  $\mathbf{L} = \mathbf{T} - \mathbf{V}$ . To make the derivation simpler, gravitational forces are considered as external forces acting on the body. Hence, potential energy vanishes and has no contribution in the Lagrangian term. Therefore, the Lagrangian term only depends on the kinetic energy of the system.

The external force vector  $\{ {}^b\mathbf{F}_B \} = \{ {}^b\mathbf{F}_a \} + \{ {}^b\mathbf{F}_g \}$  where  $\{ {}^b\mathbf{F}_a \}$  is the aerodynamic force vector and  $\{ {}^b\mathbf{F}_g \}$  is the gravitational force vector. While the external moment vector  $\{ {}^b\mathbf{M}_B \} = \{ {}^b\mathbf{M}_a \} + \{ {}^b\mathbf{M}_g \}$  where  $\{ {}^b\mathbf{M}_a \}$  is the aerodynamic moment vector and  $\{ {}^b\mathbf{M}_g \}$  is the gravitational moment vector.

## 2.5 Gravitational loads

The gravitational loads of the body and the two wings are considered. Gravitational forces act in the inertial  $z_i$  at each corresponding center of mass and the total gravitational force vector is expressed as follows

$$\{ {}^i\mathbf{F}_g \} = \{ {}^i\mathbf{F}_{g_B} \} + \{ {}^i\mathbf{F}_{g_{W_r}} \} + \{ {}^i\mathbf{F}_{g_{W_l}} \} \quad (30)$$

$$\{ {}^i\mathbf{F}_g \} = \begin{Bmatrix} 0 \\ 0 \\ (m_B + m_{W_r} + m_{W_l}) g_c \end{Bmatrix} \quad (31)$$

where  $g_c$  is the gravitational acceleration constant. While  ${}^i\mathbf{F}_g$  expressed in the body frame as

$$\{ {}^b\mathbf{F}_g \} = [\mathbf{R}_i^b] \{ {}^i\mathbf{F}_g \} \quad (32)$$

Wing gravitational loads produce gravitational moment about the body center of mass, expressed in the body frame as shown in the following equation

$$\begin{aligned} \{ {}^b\mathbf{M}_g \} &= ({}^b\mathbf{r}_{H_r}^B + {}^b\mathbf{r}_{W_r}^{H_r}) \times \{ {}^b\mathbf{F}_{g_{W_r}} \} + ({}^b\mathbf{r}_{H_l}^B + {}^b\mathbf{r}_{W_l}^{H_l}) \\ &\quad \times \{ {}^b\mathbf{F}_{g_{W_l}} \} \end{aligned} \quad (33)$$

## 2.6 Aerodynamic modeling

The aerodynamic model is derived based on quasi-steady assumptions. LEV and rotational circulation are taken into account. The aerodynamic loads considered are those produced from the airflow around the wings only, due to high flapping frequency and low body velocity in the hovering conditions.

Translation motion of the wing produces lift and drag forces that can be described as follows

$$dL_T = \frac{1}{2} \rho C_L(\alpha) v^2(r) c(r) dr \quad (34)$$

$$dD_T = \frac{1}{2} \rho C_D(\alpha) v^2(r) c(r) dr \quad (35)$$

where  $\rho$  is the density of air,  $C_L(\alpha)$  and  $C_D(\alpha)$  are the coefficients of lift and drag, respectively,  $c(r)$  is the section chord, and  $v(r)$  is the translation velocity of the wing section.

Formulas of lift and drag coefficients are given by Dickinson et al. [7] as follows

$$C_L(\alpha) = 0.225 + 1.58 \sin(2.13\alpha - 7.20) \quad (36)$$

$$C_D(\alpha) = 1.920 - 1.55 \cos(2.04\alpha - 9.82) \quad (37)$$

where  $\alpha$  is the angle of attack in degrees. By integrating Eqs. (34 and 35) over wing span and taking  $v(r) = r\dot{\kappa}$ , the lift and drag forces can be obtained

$$L_T = K_L(\alpha) \dot{\kappa}^2 \quad (38)$$



$$D_T = K_D(\alpha)\dot{\kappa}^2 \quad (39)$$

where  $K_L(\alpha) = K C_L(\alpha)$  and  $K_D(\alpha) = K C_D(\alpha)$  with constant  $K = \frac{1}{2}\rho \int_0^R r^2 c(r) dr$

According to Dickinson et al. [7], the rotation circulation per unit span is given by

$$\Gamma_R = \pi \omega c^2(r) \left( \frac{3}{4} - \hat{x}_o \right) \quad (40)$$

where  $\omega$  is the angular velocity of the wing rotation about span axis, and  $\hat{x}_o$ , chosen to be 1/4, is the normalized distance from leading edge to the rotation axis of the wing.

According to the Kutta–Joukowski theorem, the rotational force is defined as

$$F_R = \rho v(r) \Gamma_R \quad (41)$$

By integrating over the wing span, taking  $\omega = \dot{\tau}$  for both wings gives the rotational forces as

$$F_{R,r} = -K_R \dot{\kappa}_r \dot{\tau} \quad (42)$$

$$F_{R,l} = K_R \dot{\kappa}_l \dot{\tau} \quad (43)$$

where  $K_R = \frac{1}{2}\pi\rho \int_0^R r c^2(r) dr$

The rotational force acts normal to the wing section. Therefore, it can be resolved using the angle of attack into two components, lift and drag, as shown

$$L_R = F_R \cos(\alpha) \quad (44)$$

$$D_R = F_R \sin(\alpha) \quad (45)$$

The angle of attack  $\alpha$  is defined as a function of the feathering angle  $\tau$  and the direction of flapping velocity  $\dot{\kappa}$  as follows

$$\alpha_r = \begin{cases} \pi - \tau_r & \dot{\kappa}_r > 0 \\ \tau_r & \dot{\kappa}_r < 0 \end{cases} \quad \alpha_l = \begin{cases} \tau_l & \dot{\kappa}_l > 0 \\ \pi - \tau_l & \dot{\kappa}_l < 0 \end{cases} \quad (46)$$

The total lift and drag forces, for each wing, can be expressed as the summation of the components caused by each translation and rotation motions, expressed for the right wing as

$$\begin{aligned} L_{\text{tot},r} &= L_{\text{trans},r} + L_{\text{rot},r} \\ L_{\text{trans},r} &= K_L(\alpha_r)\dot{\kappa}_r^2, \quad L_{\text{rot},r} = -K_R \dot{\kappa}_r \dot{\tau} \cos \alpha_r \\ D_{\text{tot},r} &= D_{\text{trans},r} + D_{\text{rot},r} \\ D_{\text{trans},r} &= K_D(\alpha_r)\dot{\kappa}_r^2, \quad D_{\text{rot},r} = -K_R \dot{\kappa}_r \dot{\tau} \sin \alpha_r \end{aligned}$$

and the left wing as

$$L_{\text{tot},l} = L_{\text{trans},l} + L_{\text{rot},l}$$

$$L_{\text{trans},l} = K_L(\alpha_l)\dot{\kappa}_l^2, \quad L_{\text{rot},l} = K_R \dot{\kappa}_l \dot{\tau} \cos \alpha_l$$

$$D_{\text{tot},l} = D_{\text{trans},l} + D_{\text{rot},l}$$

$$D_{\text{trans},l} = K_D(\alpha_l)\dot{\kappa}_l^2, \quad D_{\text{rot},l} = K_R \dot{\kappa}_l \dot{\tau} \sin \alpha_l$$

The total aerodynamic force, expressed in the body frame, for each wing is expressed as

$$\begin{aligned} {}^b\mathbf{F}_{W_{r,a}} &= \begin{bmatrix} D_{\text{tot},r} \sin(\kappa_r) \cos(\mu_r) - L_{\text{tot},r} \sin(\mu_r) \\ D_{\text{tot},r} \sin(\kappa_r) \sin(\mu_r) \\ -D_{\text{tot},r} \cos(\kappa_r) \sin(\mu_r) - L_{\text{tot},r} \cos(\mu_r) \end{bmatrix} \\ {}^b\mathbf{F}_{W_{l,a}} &= \begin{bmatrix} -D_{\text{tot},l} \sin(\kappa_l) \cos(\mu_l) - L_{\text{tot},l} \sin(\mu_l) \\ -D_{\text{tot},l} \sin(\kappa_l) \sin(\mu_l) \\ D_{\text{tot},l} \sin(\kappa_l) \cos(\mu_l) - L_{\text{tot},l} \cos(\mu_l) \end{bmatrix} \end{aligned}$$

The total aerodynamic force vector acting on the FWMAV is the sum of the forces produced by the two wings,

$${}^b\mathbf{F}_a = {}^b\mathbf{F}_{W_{r,a}} + {}^b\mathbf{F}_{W_{l,a}} \quad (47)$$

The total aerodynamic force acts at the center of pressure (cp) point on each wing. Position vectors of the translational and rotational centers of pressure to the hinge center of mass is defined as follows

$$\begin{aligned} \mathbf{r}_{\text{cp}_{\text{rot},r}}^{H_r} &= \{0, y_{\text{cp}_{\text{rot}}}, 0\}^T, \\ \mathbf{r}_{\text{cp}_{\text{trans},r}}^{H_r} &= \{0, y_{\text{cp}_{\text{trans}}}, 0\}^T \\ \mathbf{r}_{\text{cp}_{\text{rot},l}}^{H_l} &= \{0, -y_{\text{cp}_{\text{rot}}}, 0\}^T, \\ \mathbf{r}_{\text{cp}_{\text{trans},l}}^{H_l} &= \{0, -y_{\text{cp}_{\text{trans}}}, 0\}^T \end{aligned}$$

where  $y_{\text{cp}_{\text{rot}}}$  and  $y_{\text{cp}_{\text{trans}}}$  can be calculated using the following formulas [14]

$$y_{\text{cp}_{\text{rot}}} = \frac{\int_0^R r^2 c^2(r) dr}{\int_0^R r c^2(r) dr}, \quad y_{\text{cp}_{\text{trans}}} = \frac{\int_0^R r^3 c(r) dr}{\int_0^R r^2 c(r) dr}$$

Consequently, the position vector from the corresponding center of pressure points to the body center of mass for both wings can be defined as

$${}^b\mathbf{r}_{\text{cp}_{\text{rot}}}^B = {}^b\mathbf{r}_H^B + {}^b\mathbf{r}_{\text{cp}_{\text{rot}}}^H, \quad {}^b\mathbf{r}_{\text{cp}_{\text{trans}}}^B = {}^b\mathbf{r}_H^B + {}^b\mathbf{r}_{\text{cp}_{\text{trans}}}^H$$

Finally, the aerodynamic moment can be expressed as

$$\begin{aligned} {}^b\mathbf{M}_a &= {}^b\mathbf{r}_{\text{cp}_{\text{trans},r}}^B \times {}^b\mathbf{F}_{W_{r,a}\text{trans}} + {}^b\mathbf{r}_{\text{cp}_{\text{rot},r}}^B \times {}^b\mathbf{F}_{W_{r,a}\text{rot}} \\ &\quad + {}^b\mathbf{r}_{\text{cp}_{\text{trans},l}}^B \times {}^b\mathbf{F}_{W_{l,a}\text{trans}} + {}^b\mathbf{r}_{\text{cp}_{\text{rot},l}}^B \times {}^b\mathbf{F}_{W_{l,a}\text{rot}} \end{aligned} \quad (48)$$

where  ${}^b\mathbf{F}_{W_{r,a_{\text{trans}}}}$  and  ${}^b\mathbf{F}_{W_{r,a_{\text{rot}}}}$  are the translational and rotational components of the total aerodynamic force of the right wing, respectively. While  ${}^b\mathbf{F}_{W_{l,a_{\text{trans}}}}$  and  ${}^b\mathbf{F}_{W_{l,a_{\text{rot}}}}$  are the same components for the left wing.

### 3 Control oriented model

The dynamic model of the FWMAV was formulated in the previous section. The model is nonlinear time-varying coupled system, which makes the controller design with present conditions very difficult. A control oriented model is discussed in this section to facilitate controller design. Some assumptions will be applied during controller design. Also, averaging techniques will be applied for the periodic aerodynamic loads, yielding a time-invariant system.

The model presented in this work mimics the model of Harvard Robofly [23], having wing inertia and mass parameters of negligible order compared to that of the body. Hence, wing mass and inertia effects on the body will be neglected during controller synthesis.

#### 3.1 Translation equations of motion

Translation equations of motion can be expressed in the body frame as follows

$$\{{}^b\dot{\mathbf{v}}_B^O\} = [\mathbf{M}]^{-1} [\mathbf{F}_a + \mathbf{F}_g + \mathbf{f}(u, v, w)] \quad (49)$$

Equation (49) is expanded and can be displayed in the matrix form as

$$\begin{Bmatrix} \dot{u} \\ \dot{v} \\ \dot{w} \end{Bmatrix} = \begin{bmatrix} m_B & 0 & 0 \\ 0 & m_B & 0 \\ 0 & 0 & m_B \end{bmatrix}^{-1} \begin{Bmatrix} F_{ax} + F_{gx} + f_1 \\ F_{ay} + F_{gy} + f_2 \\ F_{az} + F_{gz} + f_3 \end{Bmatrix} \quad (50)$$

where

$$\begin{aligned} f_1 &= m_B (r v - q w) \\ f_2 &= m_B (r u - p w) \\ f_3 &= m_B (q u - p v) \end{aligned}$$

Following the definition of inertial frame velocity vector found in Eq. (5), the acceleration vector is

$$\{{}^i\ddot{\mathbf{r}}_B^O\} = [\mathbf{R}_b^i] \{{}^b\dot{\mathbf{v}}_B^O\} + [\dot{\mathbf{R}}_b^i] \{{}^b\mathbf{v}_B^O\} \quad (51)$$

By replacing  $\{{}^b\dot{\mathbf{v}}_B^O\}$  from Eq. (49), the translational equations of motion in the inertial frame is obtained.

#### 3.2 Rotational equations of motion

Rotational motion can be expressed in the same manner. They can be expressed in the body frame as follows

$$\{{}^b\dot{\boldsymbol{\omega}}_b^i\} = [\mathbf{I}]^{-1} [\mathbf{M}_a + \mathbf{M}_g + \mathbf{f}(p, q, r)] \quad (52)$$

Putting the previous equation in matrix form yields

$$\begin{Bmatrix} \dot{p} \\ \dot{q} \\ \dot{r} \end{Bmatrix} = \begin{bmatrix} I_{x_B} & 0 & 0 \\ 0 & I_{y_B} & 0 \\ 0 & 0 & I_{z_B} \end{bmatrix}^{-1} \begin{Bmatrix} M_{ax} + M_{gx} + f_4 \\ M_{ay} + M_{gy} + f_5 \\ M_{az} + M_{gz} + f_6 \end{Bmatrix} \quad (53)$$

where

$$f_4 = I_{y_B} q r - I_{z_B} p r$$

$$f_5 = I_{z_B} p r - I_{x_B} p r$$

$$f_6 = I_{x_B} p q - I_{y_B} p q$$

while gravitational moments  $M_{gx}$ ,  $M_{gy}$  and  $M_{gz}$  will reduce to zero after wing inertia neglectation.

By differentiating the angular velocity in the inertial frame which was previously defined in Eq. (7), with respect to time. The rotational acceleration can be obtained as follows

$$\{\ddot{\boldsymbol{\varphi}}\} = [\dot{\mathbf{E}}_i^b]^{-1} \{{}^b\boldsymbol{\omega}_b^i\} + [\mathbf{E}_i^b]^{-1} \{{}^b\dot{\boldsymbol{\omega}}_b^i\} \quad (54)$$

By replacing  $\{{}^b\dot{\boldsymbol{\omega}}_b^i\}$  from Eq. (52), rotational equations of motion in the inertial frame can be obtained.

#### 3.3 Inertial frame equations of motion

According to the previous definitions, the equations of motion are

$$\begin{aligned} \ddot{x} &= \frac{F_{ax}}{m_B} (\cos \theta \cos \psi) \\ &+ \frac{F_{ay}}{m_B} (\sin \phi \sin \theta \cos \psi - \cos \phi \sin \psi) \\ &+ \frac{F_{az}}{m_B} (\cos \phi \sin \theta \cos \psi + \sin \phi \sin \psi) \end{aligned} \quad (55)$$

$$\begin{aligned} \ddot{y} &= \frac{F_{ax}}{m_B} (\cos \theta \sin \psi) \\ &+ \frac{F_{ay}}{m_B} (\sin \phi \sin \theta \sin \psi + \cos \phi \cos \psi) \\ &+ \frac{F_{az}}{m_B} (\cos \phi \sin \theta \sin \psi - \sin \phi \cos \psi) \end{aligned} \quad (56)$$

$$\ddot{z} = -\frac{F_{ax}}{m_B} (\sin \theta) + \frac{F_{ay}}{m_B} (\sin \phi \cos \theta)$$



$$+ \frac{F_{az}}{m_B} (\cos \phi \cos \theta) + g_c \quad (57)$$

$$\begin{aligned} \ddot{\phi} = & \frac{M_{ax}}{I_{x_B}} + \frac{M_{ay}}{I_{y_B}} (\sin \phi \tan \theta) + \frac{M_{az}}{I_{z_B}} (\cos \phi \tan \theta) \\ & + \frac{I_{y_B} - I_{z_B}}{I_{x_B}} (qr) + \frac{I_{z_B} - I_{x_B}}{I_{y_B}} (pr \sin \phi \tan \theta) \\ & + \frac{I_{x_B} - I_{y_B}}{I_{z_B}} (pq \cos \phi \tan \theta) + \dot{\phi} \dot{\theta} \tan \theta \\ & + \dot{\theta} \dot{\psi} \sec \theta \end{aligned} \quad (58)$$

$$\begin{aligned} \ddot{\theta} = & \frac{M_{ay}}{I_{y_B}} (\cos \phi) - \frac{M_{az}}{I_{z_B}} (\sin \phi) \\ & + \frac{I_{z_B} - I_{x_B}}{I_{y_B}} (pr \cos \phi) \\ & + \frac{I_{y_B} - I_{x_B}}{I_{z_B}} (pq \sin \phi) \\ & + \dot{\phi} \dot{\psi} \cos \theta \end{aligned} \quad (59)$$

$$\begin{aligned} \ddot{\psi} = & \frac{M_{ay}}{I_{y_B}} (\sin \phi \sec \theta) + \frac{M_{az}}{I_{z_B}} (\cos \phi \sec \theta) \\ & + \frac{I_{z_B} - I_{x_B}}{I_{y_B}} (pr \sin \phi \sec \theta) \\ & + \frac{I_{x_B} - I_{y_B}}{I_{z_B}} (pq \cos \phi \sec \theta) \\ & + \dot{\phi} \dot{\theta} \sec \theta + \dot{\theta} \dot{\psi} \tan \theta \end{aligned} \quad (60)$$

where all the aerodynamic forces and moments are expressed in the body frame, while  $p$ ,  $q$  and  $r$  are components of  $\{^b \omega_b^i\}$

### 3.4 Model averaging

In this section, averaging of the aerodynamic model over a single wing beat will be presented. Averaging will be applied to obtain a time-invariant model suitable for control synthesis.

Model averaging in this work is adopted from Kalliny et al. [14]. A new time scale and its time derivative are defined as follows

$$T = \omega_o t + \phi \quad \dot{T} = \omega_o (1 + \delta)^2 \quad (61)$$

The new time scale is plugged in the system equations and consequently the averaging parameter  $\epsilon$  is chosen as  $\frac{1}{\omega_o}$  having  $\omega_o \gg 1$ .

Aerodynamic loads are averaged according to the averaging function defined as follows

$$\bar{F}_{av} = \frac{1}{2\pi} \int_0^{2\pi} F(T, u, \epsilon) dT \quad (62)$$

where  $\bar{F}_{av}$  is the cycle-average of  $F$  with  $T$  being the previously defined new time scale,  $u$  is the control parameters vector and  $\epsilon$  being the averaging parameter.

Cycle-averaging yields the following averaged aerodynamic loads

$$\begin{aligned} {}^b \bar{F}_{ax} = & -G_1 \pi^2 \left( \sin(\mu_l) (1 + \delta_l)^2 \right. \\ & \left. + \sin(\mu_r) (1 + \delta_r)^2 \right) \end{aligned} \quad (63)$$

$${}^b \bar{F}_{ay} = 0 \quad (64)$$

$$\begin{aligned} {}^b \bar{F}_{az} = & -G_1 \pi^2 \left( \cos(\mu_l) (1 + \delta_l)^2 \right. \\ & \left. + \cos(\mu_r) (1 + \delta_r)^2 \right) \end{aligned} \quad (65)$$

$$\begin{aligned} {}^b \bar{M}_{ax} = & G_1 \left( \cos(\mu_l) (1 + \delta_l)^2 - \cos(\mu_r) (1 + \delta_r)^2 \right) \\ & \left( C_I y_{cpt} \cos(\beta) + \pi^2 y_H \right) \end{aligned} \quad (66)$$

$$\begin{aligned} {}^b \bar{M}_{ay} = & G_1 \left( (C_I y_{cpt} \sin(\beta) ((1 + \delta_l)^2 + (1 + \delta_r)^2) \right. \\ & \left. + (\pi^2 z_H (\sin(\mu_l) (1 + \delta_l)^2 \right. \\ & \left. + \sin(\mu_r) (1 + \delta_r)^2)) \right) \end{aligned} \quad (67)$$

$$\begin{aligned} {}^b \bar{M}_{az} = & -G_1 \left( \sin(\mu_l) (1 + \delta_l)^2 - \sin(\mu_r) (1 + \delta_r)^2 \right) \\ & \left( C_I y_{cpt} \cos(\beta) + \pi^2 y_H \right) \end{aligned} \quad (68)$$

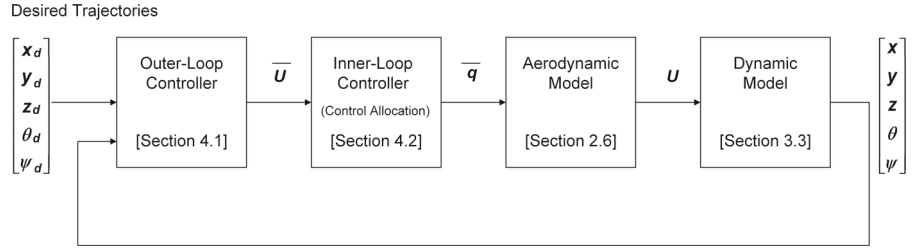
where  $G_1 = \frac{1}{18} \omega_o^2 K_L(\alpha_l)$   $C_I = 8.57713$

### 3.5 Control derivatives

The control parameters responsible for manipulating cycle-averaged forces and moments are the variation of flapping frequency for both wings  $\delta_l$  and  $\delta_r$ , biasing angle  $\beta$  and stroke plane angles for both wings  $\mu_l$  and  $\mu_r$ . For control authority analysis, the sensitivity of the cycle-averaged forces and moments to each control parameter is evaluated. Partial derivatives of each of the cycle-averaged forces and moments with respect to each control parameter is calculated [19] using Eqs. (63)–(68). The control derivatives are evaluated in details in “Appendix A”.

### 3.6 Hovering conditions

The control derivatives are evaluated about hover. At hovering condition, the lift force must equal the

**Fig. 4** Control architecture

vehicle's weight. By satisfying Eq. (65) as well as ensuring symmetric wing motion which is given by  $[\delta_l, \delta_r, \beta, \mu_l, \mu_r] = [0, 0, 0, 0, 0]$  and all other forces and moments would equal to zero. Hence,  $\omega_o$  can be calculated as

$$\omega_o = \sqrt{\frac{m_B g_c}{K_L'}} \quad (69)$$

where  $K_L' = \frac{\pi^2}{9} K_L(\alpha)$

### 3.7 Control effectiveness matrix

The desired cycle-averaged forces and moments commands can be expressed in terms of the control parameters in the following form

$$\begin{bmatrix} \Delta^b \bar{F}_{ax} \\ \Delta^b \bar{F}_{ay} \\ \Delta^b \bar{F}_{az} \\ \Delta^b \bar{M}_{ax} \\ \Delta^b \bar{M}_{ay} \\ \Delta^b \bar{M}_{az} \end{bmatrix} = \mathbf{CEM} \begin{bmatrix} \delta_l \\ \delta_r \\ \beta \\ \mu_l \\ \mu_r \end{bmatrix}$$

where **CEM** is the control effectiveness matrix expressed as [20]

$$\mathbf{CEM} = \begin{bmatrix} \frac{\partial^b \bar{F}_{ax}}{\partial \delta_l} & \frac{\partial^b \bar{F}_{ax}}{\partial \delta_r} & \frac{\partial^b \bar{F}_{ax}}{\partial \beta} & \frac{\partial^b \bar{F}_{ax}}{\partial \mu_l} & \frac{\partial^b \bar{F}_{ax}}{\partial \mu_r} \\ \frac{\partial^b \bar{F}_{ay}}{\partial \delta_l} & \frac{\partial^b \bar{F}_{ay}}{\partial \delta_r} & \frac{\partial^b \bar{F}_{ay}}{\partial \beta} & \frac{\partial^b \bar{F}_{ay}}{\partial \mu_l} & \frac{\partial^b \bar{F}_{ay}}{\partial \mu_r} \\ \frac{\partial^b \bar{F}_{az}}{\partial \delta_l} & \frac{\partial^b \bar{F}_{az}}{\partial \delta_r} & \frac{\partial^b \bar{F}_{az}}{\partial \beta} & \frac{\partial^b \bar{F}_{az}}{\partial \mu_l} & \frac{\partial^b \bar{F}_{az}}{\partial \mu_r} \\ \frac{\partial^b \bar{M}_{ax}}{\partial \delta_l} & \frac{\partial^b \bar{M}_{ax}}{\partial \delta_r} & \frac{\partial^b \bar{M}_{ax}}{\partial \beta} & \frac{\partial^b \bar{M}_{ax}}{\partial \mu_l} & \frac{\partial^b \bar{M}_{ax}}{\partial \mu_r} \\ \frac{\partial^b \bar{M}_{ay}}{\partial \delta_l} & \frac{\partial^b \bar{M}_{ay}}{\partial \delta_r} & \frac{\partial^b \bar{M}_{ay}}{\partial \beta} & \frac{\partial^b \bar{M}_{ay}}{\partial \mu_l} & \frac{\partial^b \bar{M}_{ay}}{\partial \mu_r} \\ \frac{\partial^b \bar{M}_{az}}{\partial \delta_l} & \frac{\partial^b \bar{M}_{az}}{\partial \delta_r} & \frac{\partial^b \bar{M}_{az}}{\partial \beta} & \frac{\partial^b \bar{M}_{az}}{\partial \mu_l} & \frac{\partial^b \bar{M}_{az}}{\partial \mu_r} \end{bmatrix} \quad (70)$$

**CEM** provides information on how variation in control parameters affect cycle-averaged aerodynamic forces and moments. By substituting with the control derivatives evaluated about hover, the control effectiveness matrix is evaluated. The rank of the **CEM** was found to be five, since it is not possible to generate direct side

forces in  $Y$ -body axis direction. Hence, five-DOF control authority is provided by the chosen control parameters.

## 4 Controller design

The control objective is to perform trajectory tracking under six-DOF simulation, utilizing the available five-DOF control authority discussed in Sect. 3.7. The control oriented model presented in Sect. 3 is used here for designing position and attitude trajectory tracking control law, employing two control loops as shown in Fig. 4. The outer-loop control illustrated in Sect. 4.1 and inner-loop control found in Sect. 4.2.

### 4.1 Outer-loop controller design

The outer-loop controller adjusts the position and attitude of the vehicle, with respect to the inertial frame, to track a given desired trajectory. The control strategy is to utilize the cycle-averaged aerodynamic forces and moments as virtual control inputs. The outer-loop control law produces the desired cycle-averaged forces and moments. For that purpose, the FWMAV model is divided into three subsystems,  $X-Z$ ,  $Y-\phi$  and  $\theta-\psi$  subsystems. A block diagram of the outer-loop controller is shown in Fig. 5.

#### Control algorithm

The equations of motion for each subsystem will be presented in the state-space form as follows

$$\dot{x} = f(x) + g(x)u \quad (71)$$

where  $x$  is  $n$ -dimensional state vector and  $u$  is  $p$ -dimensional input vector. While  $f(x)$  is  $n$ -dimensional vector and  $g(x)$  is  $(n \times p)$  matrix of nonlinear coefficients  $g_{ij}$ .

Considering the sliding surface definition as [10]

$$S = [S_1, \dots, S_p]^T \quad (72)$$

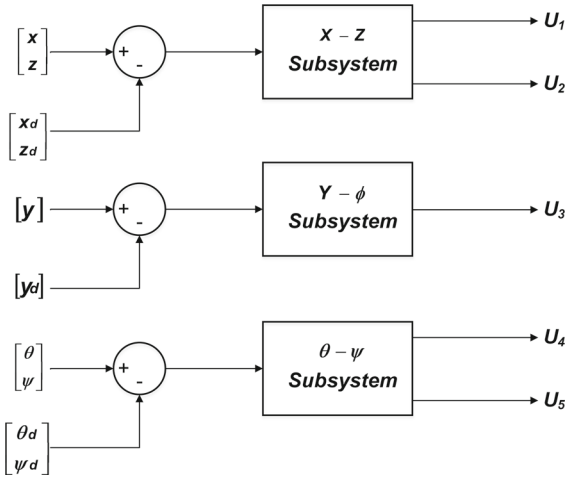


**Fig. 5** Outer-loop controller block diagram

where  $S_i$  is defined by

$$S_i = \dot{e}_i + 2\lambda_i e_i + \lambda_i^2 \int_0^t e_i d\tau - \dot{e}_i(0) - 2\lambda_i e_i(0) \quad (73)$$

where  $e_i = x_i - x_{i_d}$  is the tracking error and  $\lambda_i$  is a positive constant [22], knowing that the relative degree of the sliding surface is 2.

The sliding variable time derivative  $\dot{S}_i$  can be expressed as [2]

$$\dot{S}_i = h_i + b_{i1}u_1 + \dots + b_{ip}u_p = h_i + \sum_{k=1}^p b_{ik}u_k \quad (74)$$

with

$$h_i = \frac{\partial S_i}{\partial t} + \sum_{j=1}^n \frac{\partial S_i}{\partial x_j} f_j \quad (75)$$

while

$$b_{ik} = \sum_{j=1}^n \frac{\partial S_i}{\partial x_j} g_{jk} \quad (76)$$

Consequently  $\dot{S}$  can be expressed as

$$\dot{S} = h + bu \quad (77)$$

$$\text{where } h = [h_1, \dots, h_p]^T \text{ and } b = \begin{bmatrix} b_{11} & \dots & b_{1p} \\ \vdots & \ddots & \vdots \\ b_{p1} & \dots & b_{pp} \end{bmatrix}$$

The control law for ISMC so that the sliding surfaces go to zero in a finite time is defined by

$$u = -b^{-1} \left( h + \begin{bmatrix} K_1 \text{sign}(S_1) \\ \vdots \\ K_p \text{sign}(S_p) \end{bmatrix} \right) \quad (78)$$

where  $K_1, \dots, K_p$  are positive constants and  $b$  is invertible.

Consider the following Lyapunov function

$$V = \frac{1}{2} S^T S \quad (79)$$

The derivative of Lyapunov function is given by

$$\dot{V} = S^T \dot{S} = S^T (h + bu) \quad (80)$$

By applying the control law from Eq. (78) in Eq. (80), the expression of  $\dot{V}$  yields

$$\dot{V} = -S^T \begin{bmatrix} K_1 \text{sign}(S_1) \\ \vdots \\ K_p \text{sign}(S_p) \end{bmatrix} \quad (81)$$

$$\dot{V} = -K_1 |S_1| - \dots - K_p |S_p| \leq 0 \quad (82)$$

which implies that the Lyapunov function is asymptotically stable and all the sliding surfaces tend to zero in finite time.

*X-Z subsystem*

The X-Z subsystem is a fully actuated subsystem, having two control inputs  ${}^b\overline{F}_{ax}$  and  ${}^b\overline{F}_{az}$  denoted as  $U_1$  and  $U_2$ , respectively. Considering  $x$  and  $z$  positions and their time derivatives to be the subsystem states, the state-space equations are presented as follows

$$\dot{x}_i = f_i(x) + g_{i1}(x)u_1 + g_{i2}(x)u_2 \quad (83)$$

where  $u_1$  and  $u_2$  are the subsystem inputs.

Equations (55) and (57) are represented in the state-space form

$$f_1 = x_2 \quad f_2 = 0 \quad f_3 = x_4 \quad f_4 = g_c$$

$$\begin{aligned} g_{11} &= 0 & g_{12} &= 0 \\ g_{21} &= \frac{\cos \theta \cos \psi}{m_B} & g_{22} &= \frac{\cos \phi \sin \theta \cos \psi + \sin \phi \sin \psi}{m_B} \\ g_{31} &= 0 & g_{32} &= 0 \\ g_{41} &= \frac{-\sin \theta}{m_B} & g_{42} &= \frac{\cos \phi \cos \theta}{m_B} \end{aligned}$$

where  $\{x_1, x_2, x_3, x_4\}$  are  $\{x, \dot{x}, z, \dot{z}\}$ . The outputs of this subsystem are  $x$  and  $z$  positions, being states  $x_1$  and  $x_3$ , having relative degree 2.

Consider the following sliding surface definition according to Eqs. (72), (73)

$$S = [S_1, S_2]^T$$

where  $S_1$  and  $S_2$  are the sliding surfaces of  $x$  and  $z$  positions, respectively. The integral sliding surface is defined as

$$S_1 = \dot{e}_1 + 2\lambda_1 e_1 + \lambda_1^2 \int_0^t e_1 d\tau - \dot{e}_1(0) - 2\lambda_1 e_1(0) \quad (84)$$

$$S_2 = \dot{e}_2 + 2\lambda_2 e_2 + \lambda_2^2 \int_0^t e_2 d\tau - \dot{e}_2(0) - 2\lambda_2 e_2(0) \quad (85)$$

where  $e_1 = x - x_d$  and  $e_2 = z - z_d$  are the tracking errors for  $x$  and  $z$  positions, respectively.

While  $\lambda_1, \lambda_2$  are positive gain constants.

$\dot{S}$  is expressed according to Eq. (77) where

$$\begin{aligned} h &= [h_1, h_2]^T \\ h_1 &= -\ddot{x}_d + 2\lambda_1 \dot{e}_1 + \lambda_1^2 e_1 \\ h_2 &= -\ddot{z}_d + 2\lambda_2 \dot{e}_2 + \lambda_2^2 e_2 + f_4 \\ \text{while } b &= \begin{bmatrix} b_{11} & b_{12} \\ b_{21} & b_{22} \end{bmatrix} \end{aligned}$$

$$b_{11} = g_{21} \quad b_{12} = g_{22} \quad b_{21} = g_{41} \quad b_{22} = g_{42}$$

Consequently, the control law is given by

$$u = -b^{-1} \left( h + \begin{bmatrix} K_1 \text{sign}(S_1) \\ K_2 \text{sign}(S_2) \end{bmatrix} \right) \quad (86)$$

where  $u = [U_1, U_2]^T$

Using the Lyapunov analysis discussed in Eqs. (79)–(82), one can conclude that the sliding surfaces will tend to zero. Consequently the tracking errors will converge to zero in finite time.

*Y- $\phi$  subsystem*

The  $Y$ - $\phi$  subsystem is under-actuated subsystem, having one control input  ${}^b\overline{M}_{ax}$ , denoted here as  $U_3$ . As mentioned in Sect. 3.7 side forces cannot be directly generated by the vehicle. Consequently, the rolling moment  $U_3$  is manipulated to adjust the lift forces generated by the vehicle toward the desired position in the inertial frame. Finally, the rolling angle is regulated.

Averaged form of Eq. (56) reduces to

$$\begin{aligned} \ddot{y} &= \frac{F_{ax}}{m_B} (\cos \theta \sin \psi) \\ &+ \frac{F_{az}}{m_B} (\cos \phi \sin \theta \sin \psi - \sin \phi \cos \psi) \end{aligned} \quad (87)$$

where zero side force is assumed. Vehicle's orientation indicate that at zero pitch and yaw rotation, the force directed along the inertial  $Y$ -axis reduces to

$$\ddot{y} = -\frac{F_{az}}{m_B} (\sin \phi) = v \quad (88)$$

Assuming a nominal value for the lift force  $F_{az}$  equal to the vehicle's weight  $m_B \times g_c$ , a desired roll angle  $\phi$  can be generated as an estimate for the side force command

$$\phi_d = -\arcsin\left(\frac{v}{g_c}\right) \quad (89)$$

where  $v$  is chosen as  $v = \ddot{y}_d - k_{y1} \dot{e}_y - k_{y0} e_y$  ensuring asymptotic convergence of the tracking error defined as  $e_y = y - y_d$ . The desired roll is fed through second-order filter to ensure differential continuity of the command signal and smooth its derivatives [9].

Taking the same assumptions, the rolling dynamics in Eq. (58) can be represented in the state-space form as

$$\dot{x}_i = f_i(x) + g_i(x) u \quad (90)$$

where

$$\begin{aligned} f_1 &= x_2 & f_2 &= ((I_{yB} - I_{zB})/I_{x_B})(qr) + \dot{\theta} \dot{\psi} \\ g_1 &= 0 & g_2 &= 1/I_{x_B} \end{aligned}$$

where  $\{x_1, x_2\}$  are  $\{\phi, \dot{\phi}\}$ . The sliding surface  $S_3$  is defined similar to Eq. (73), where the tracking error for this subsystem is  $e_3 = \phi - \phi_d = x_1 - x_{1d}$

Similar to Eq. (78) the ISMC law is designed as follows

$$u = -b_3^{-1} (h_3 + K_3 \text{sign}(S_3)) \quad (91)$$

where  $h_3 = -\ddot{\phi}_d + 2\lambda_3 \dot{e}_3 + \lambda_3^2 e_3 + f_2$  and  $b_3 = g_2$  while  $u$  is denoted as  $U_3$

Using Lyapunov analysis in Eqs. (79)–(82), it is concluded that the rolling angle  $\phi$  will converge to its desired value, commanding the  $y$  translation to its reference waypoint.

*$\theta$ - $\psi$  subsystem*

The  $\theta$ - $\psi$  subsystem is a fully actuated subsystem, having two control inputs  ${}^b\overline{M}_{ay}$  and  ${}^b\overline{M}_{az}$ , denoted as  $U_4$  and  $U_5$  respectively. The states of this subsystems are the pitching and yawing angles  $\theta$  and  $\psi$  and their time derivatives. State-space equations are presented similar to the previous subsystems

$$\dot{x}_i = f_i(x) + g_{i1}(x) u_1 + g_{i2}(x) u_2 \quad (92)$$

Eqs. (59) and (60) are represented in the state-space form as follows

$$\begin{aligned} f_1 &= x_2 & f_2 &= f_{21} + f_{22} \\ f_{21} &= \frac{I_{zB} - I_{x_B}}{I_{yB}} (pr \cos \phi) + \frac{I_{yB} - I_{x_B}}{I_{zB}} (pq \sin \phi) \end{aligned}$$

$$\begin{aligned}
 f_{22} &= \dot{\phi} x_4 \cos x_1 \\
 f_3 &= x_4 \quad f_4 = f_{41} + f_{42} \\
 f_{41} &= \left( \frac{I_{z_B} - I_{x_B}}{I_{y_B}} (pr \sin \phi) \right. \\
 &\quad \left. + \frac{I_{x_B} - I_{y_B}}{I_{z_B}} (pq \cos \phi) \right) \sec x_1 \\
 f_{42} &= \dot{\phi} x_2 \sec x_1 + x_2 x_4 \tan x_1 \\
 g_{11} &= 0 \quad g_{12} = 0 \quad g_{21} = \frac{\cos \phi}{I_{y_B}} \quad g_{22} = -\frac{\sin \phi}{I_{z_B}} \\
 g_{31} &= 0 \quad g_{32} = 0 \quad g_{41} = \frac{\sin \phi \sec x_1}{I_{y_B}} \\
 g_{42} &= \frac{\cos \phi \sec x_1}{I_{z_B}}
 \end{aligned}$$

where  $\{x_1, x_2, x_3, x_4\}$  are  $\{\theta, \dot{\theta}, \psi, \dot{\psi}\}$ . The outputs of this subsystem are  $\theta$  and  $\psi$ , having relative degree of 2. Hence, the sliding surface  $S$  is defined as

$$S = [S_4, S_5]^T$$

where  $S_4$  and  $S_5$  are defined similar to Eq. (73), while  $h$  and  $b$  are found using Eqs. (75), (76) as

$$\begin{aligned}
 h_4 &= -\ddot{\theta}_d + 2\lambda_4 \dot{e}_4 + \lambda_4^2 e_4 + f_2 \\
 h_5 &= -\ddot{\psi}_d + 2\lambda_5 \dot{e}_5 + \lambda_5^2 e_5 + f_4 \\
 b_{41} &= g_{21} \quad b_{42} = g_{22} \quad b_{51} = g_{41} \quad b_{52} = g_{42}
 \end{aligned}$$

In the same manner, SMC law is given by

$$u = -b^{-1} \left( h + \begin{bmatrix} K_4 \text{sign}(S_4) \\ K_5 \text{sign}(S_5) \end{bmatrix} \right) \quad (93)$$

where  $u = [U_4, U_5]^T$

while  $h = [h_4, h_5]^T$  and  $b = \begin{bmatrix} b_{41} & b_{42} \\ b_{51} & b_{52} \end{bmatrix}$

Carrying out Lyapunov analysis similar to Eqs. (79)–(82), it can be proved that pitch and yaw angles  $\theta$  and  $\psi$  will converge to their desired trajectory and their tracking errors will go to zero in finite time.

The discontinuous sign function used in the control law is approximated to a continuous saturation function  $\text{sat}(\cdot)$  in all previous controllers [10]. This approximation can reduce chattering associated with discontinuous control action and eliminate its undesirable effects. The  $\text{sat}(\cdot)$  is defined as follows

$$\text{sat} \left( \frac{S}{\Delta} \right) = \begin{cases} -1 & S < -\Delta \\ \frac{S}{\Delta} & -\Delta < S < \Delta \\ 1 & S > \Delta \end{cases}$$

where  $\Delta$  represents the boundary layer thickness which can be tuned to yield smoother control input. This

approximation leads to tracking within a guaranteed precision  $\epsilon$ , where  $\epsilon = \frac{\Delta}{\lambda}$  which can be tuned to achieve good tracking precision while ensuring that all the trajectories starting inside the boundary layer at  $t = 0$  will remain inside for  $t \geq 0$  and the term  $\text{sign}(S)$  is replaced by  $\frac{S}{\Delta}$  inside the boundary layer [22]. However, if an external disturbance is applied to the system which lead to separation from the boundary layer, the control law in Eq. (78) will be applied without approximation and will force the sliding variable toward the boundary layer. Moreover, the integral term adds robustness to the system which overcomes the effects of external disturbances and eliminates steady-state errors. This will be discussed in the simulation results section.

## 4.2 Inner-loop controller design

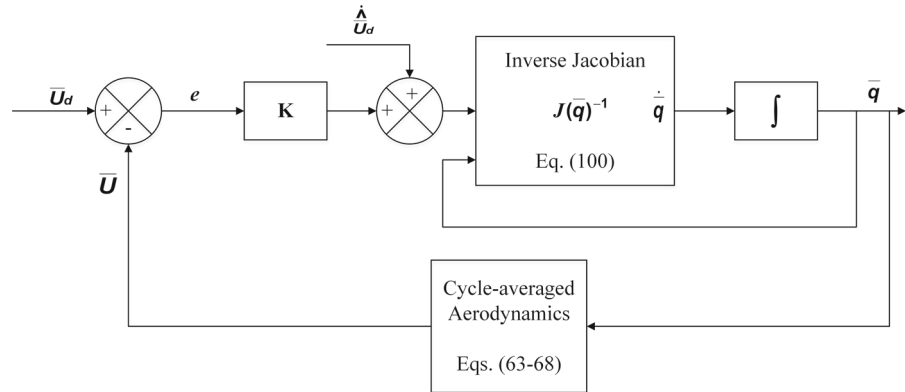
The output of the outer-loop control in Sect. 4.1 is the desired cycle-averaged forces and moments, denoted as virtual control inputs ( $U_1, U_2, U_3, U_4, U_5$ ). In order to determine the actual control parameters ( $\delta_l, \delta_r, \beta, \mu_l, \mu_r$ ), a system of nonlinear equations needs to be solved. Linear solving methods are commonly used in the literature for linearized aerodynamic loads [9]. However, these methods provide solutions limited to the region around the linearization points. Moreover, convergence to the desired values of forces and moments is not guaranteed since these techniques are open-loop mathematical methods. On the other hand, control allocation problem can be addressed using neural networks technique [1], but at the price of great computational complexity of such algorithms that require multiple iterations and huge number of computations. In the current work, accurate solutions are required for the system of nonlinear equations (63)–(68), with guaranteed convergence and reasonable computational complexity. For that purpose, a Lyapunov-based closed-loop control law is designed. It aims to stabilize the error between the desired and actual aerodynamic forces and moments utilizing control parameters. The inner loop control is presented in Fig. 6.

In order to guarantee error elimination, the following Lyapunov function  $V$  is defined as follows

$$V = \frac{1}{2} e^T e \quad (94)$$

The time derivative is given by

$$\dot{V} = e^T \dot{e} = e^T (\dot{\bar{U}}_d - \dot{\bar{U}}) \quad (95)$$

**Fig. 6** Inner-loop control

where  $\mathbf{e}$  is the error vector and can be found as

$$\mathbf{e} = \bar{\mathbf{U}}_d - \bar{\mathbf{U}} \quad (96)$$

where  $\bar{\mathbf{U}}_{5 \times 1} = [{}^b\bar{F}_{ax}, {}^b\bar{F}_{az}, {}^b\bar{M}_{ax}, {}^b\bar{M}_{ay}, {}^b\bar{M}_{az}]^T$  is the cycle-averaged aerodynamic forces and moments vector presented in Eqs. (63)–(68), and  $\bar{\mathbf{U}}_d = [U_1, U_2, U_3, U_4, U_5]^T$ , is the desired values vector.  $\bar{\mathbf{U}}$  is expressed in terms of the actual control parameters vector,  $\bar{\mathbf{q}}_{5 \times 1} = [\delta_l, \delta_r, \beta, \mu_l, \mu_r]^T$ , in the following equation

$$\bar{\mathbf{U}} = f(\bar{\mathbf{q}}) \quad (97)$$

and  $\dot{\bar{\mathbf{U}}}$  is found as

$$\dot{\bar{\mathbf{U}}} = J(\bar{\mathbf{q}}) \dot{\bar{\mathbf{q}}} \quad (98)$$

where  $J(\bar{\mathbf{q}})_{5 \times 5}$  is the Jacobian matrix of the aerodynamic loads expressions with respect to the actual control parameters, it is expressed as

$$J(\bar{\mathbf{q}}) = \begin{bmatrix} \frac{\partial {}^b\bar{F}_{ax}}{\partial \delta_l} & \frac{\partial {}^b\bar{F}_{ax}}{\partial \delta_r} & \frac{\partial {}^b\bar{F}_{ax}}{\partial \beta} & \frac{\partial {}^b\bar{F}_{ax}}{\partial \mu_l} & \frac{\partial {}^b\bar{F}_{ax}}{\partial \mu_r} \\ \frac{\partial {}^b\bar{F}_{az}}{\partial \delta_l} & \frac{\partial {}^b\bar{F}_{az}}{\partial \delta_r} & \frac{\partial {}^b\bar{F}_{az}}{\partial \beta} & \frac{\partial {}^b\bar{F}_{az}}{\partial \mu_l} & \frac{\partial {}^b\bar{F}_{az}}{\partial \mu_r} \\ \frac{\partial {}^b\bar{M}_{ax}}{\partial \delta_l} & \frac{\partial {}^b\bar{M}_{ax}}{\partial \delta_r} & \frac{\partial {}^b\bar{M}_{ax}}{\partial \beta} & \frac{\partial {}^b\bar{M}_{ax}}{\partial \mu_l} & \frac{\partial {}^b\bar{M}_{ax}}{\partial \mu_r} \\ \frac{\partial {}^b\bar{M}_{ay}}{\partial \delta_l} & \frac{\partial {}^b\bar{M}_{ay}}{\partial \delta_r} & \frac{\partial {}^b\bar{M}_{ay}}{\partial \beta} & \frac{\partial {}^b\bar{M}_{ay}}{\partial \mu_l} & \frac{\partial {}^b\bar{M}_{ay}}{\partial \mu_r} \\ \frac{\partial {}^b\bar{M}_{az}}{\partial \delta_l} & \frac{\partial {}^b\bar{M}_{az}}{\partial \delta_r} & \frac{\partial {}^b\bar{M}_{az}}{\partial \beta} & \frac{\partial {}^b\bar{M}_{az}}{\partial \mu_l} & \frac{\partial {}^b\bar{M}_{az}}{\partial \mu_r} \end{bmatrix} \quad (99)$$

The derivative of the Lyapunov function  $\dot{V}$  is found as

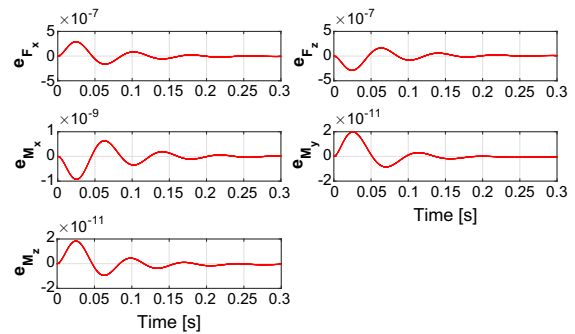
$$\dot{V} = \mathbf{e}^T (\dot{\bar{\mathbf{U}}}_d - J(\bar{\mathbf{q}}) \dot{\bar{\mathbf{q}}}) \quad (100)$$

By choosing  $\dot{\bar{\mathbf{q}}}$  as

$$\dot{\bar{\mathbf{q}}} = J(\bar{\mathbf{q}})^{-1} (\mathbf{K} \mathbf{e} + \dot{\bar{\mathbf{U}}}_d) \quad (101)$$

where  $\mathbf{K}$  is a positive definite gain matrix. This yields

$$\dot{V} = -\mathbf{e}^T \mathbf{K} \mathbf{e} \quad (102)$$

**Fig. 7** Control allocation errors

Consequently, by choosing the control action for  $\dot{\bar{\mathbf{q}}}$  in Eq. (101), the Lyapunov function time derivative  $\dot{V}$  in Eq. (102) becomes negative definite, ensuring that the error vector  $\mathbf{e}$  converges to zero in finite time. As shown in Fig. 7, the error between the desired and actual cycle-averaged forces and moments rapidly converges to zero, while the control parameters are computed by integrating  $\dot{\bar{\mathbf{q}}}$  in Eq. (101) with zero initial conditions.

The proposed method provides accurate solutions for the control parameters which create actual forces and moments for the desired maneuvers in a short transient time, as shown in Fig. 7. Similar solutions were obtained using MATLAB® nonlinear system solver “fsolve”. This method utilizes Levenberg–Marquardt and Trust-Region methods which are based on nonlinear least-squares algorithms and other iterative techniques which perform several iterations in order to provide a single solution for each sample. However, the control law in Eq. (101) provides instant solutions in each sample, while ensuring convergence to the desired values in finite time, making this method more practical and less computationally complex.



**Table 1** Model parameters used in simulation

Parameter	Value
$m_B$ (kg)	$60 \times 10^{-6}$
$m_{W_r}, m_{W_l}$ (kg)	$0.5 \times 10^{-6}$
$I_{xx}W_r, I_{xx}W_l$ (kg m <sup>2</sup> )	$24.2 \times 10^{-12}$
$I_{yy}W_r, I_{yy}W_l$ (kg m <sup>2</sup> )	$0.95 \times 10^{-12}$
$I_{zz}W_r, I_{zz}W_l$ (kg m <sup>2</sup> )	$25.15 \times 10^{-12}$
$y_H$ (m)	$2 \times 10^{-3}$
$z_H$ (m)	0
$y_W$ (m)	$6 \times 10^{-3}$
$A_k$ (rad)	$\pi/3$
$A_r$ (rad)	$\pi/4$
$\omega_0$ (rad/s)	574.946
$y_{c_{p_{trans}}}$ (m)	$9.0581 \times 10^{-6}$
$y_{c_{p_{rot}}}$ (m)	$7.75 \times 10^{-6}$

The time derivative of the virtual control inputs  $\dot{\bar{U}}_d$  is required in the design process in Eq. (101). Applying direct differentiation to this signal is not practical, since it is susceptible to noises. Hence, a second-order linear approximation differentiator is utilized

$$\dot{\bar{U}}_d = \frac{s}{(\gamma s + 1)^2} \bar{U}_d \quad (103)$$

where  $\dot{\bar{U}}_d$  is the time derivative estimate,  $s$  is the Laplace operator and  $\gamma$  is tuned to achieve better noise attenuation and smoother control effort.

## 5 Simulation results

In order to validate the designed controller, a simulation environment is implemented in MATLAB/SIMULINK® using ode45 solver. FWMAV physical parameters are adopted from those of Harvard Robofly, presented by Kalliny et al. [14] and Wood et al. [23,24]. The parameters used throughout the simulation are listed in Table 1. While the wing shape and geometry parameters are inherited from those found in Oppenheimer et al. [17,18] and Doman et al. [8]. In addition, the wing chord definition is presented by Kalliny et al. [14].

To validate the developed controller, four different simulation conditions are carried out on the FWMAV model. The target of the first simulation is to test the performance of the proposed controller and the feasibility of the control signals. It also justifies the ability

of the controller to handle different model considerations (averaged, periodic and high-fidelity models). While the second simulation evaluates the ability of the controller to achieve complex trajectory tracking for the high-fidelity model. Moreover, the third and fourth simulations validate the robustness of the controller to external disturbances and model uncertainties in the high-fidelity model.

In the first simulation shown in Fig. 8, a unity step input is given as a reference input to each of the positions while stabilizing the orientations of the high fidelity model. The step reference is fed through a sixth-order low-pass filter ( $4^6/(s+4)^6$ ), in order to preserve differential continuity of the desired trajectories. It is obvious from Fig. 8 that the controller shows good performance in attaining the desired position. It is found that the maximum tracking error of the positions at steady state, is  $9.8255 \times 10^{-5}$  m,  $3.8397 \times 10^{-9}$  m and  $7.3232 \times 10^{-6}$  m for  $x$ ,  $y$  and  $z$  positions, respectively. While the maximum tracking error of the orientations at steady state, is  $4.4988 \times 10^{-4}$  rad and  $5.3707 \times 10^{-8}$  rad for  $\theta$  and  $\psi$ , respectively. This justifies the ability of the controller to command the high-fidelity model to track reference trajectories and overcome the effects of the unmodeled dynamics that are not considered in the controller design.

Figure 9 shows the performance of the control parameters provided from the inner-loop controller in the three models (averaged, periodic and high fidelity). It is clear from Fig. 9a and b that the steady-state value of  $\delta_L$  or  $\delta_R$  in case of the high-fidelity model is higher than zero, indicating the controller response to uncertainties associated with wing mass and inertia effects. However, these effects do not exist in the averaged or the periodic model. Hence, the control effort reaches zero at hovering conditions. Figure 9c shows that minimal variation of biasing angle  $\beta$  is needed in the current simulation. Whereas  $\mu_l$  and  $\mu_R$  shown in Fig. 9d and e adjust the stroke plane so that the generated lift force can drive the  $x$  position to its desired reference. Finally, they stabilize at zero, keeping the stroke plane horizontal and the lift force vertical against the vehicle's weight, knowing that the lift force is perpendicular to the stroke plane according to the flapping and feathering mechanism utilized by the wing motion, maintaining hovering in the reached final position.

In the second simulation shown in Fig. 10, the high-fidelity model performance is assessed with a heli-

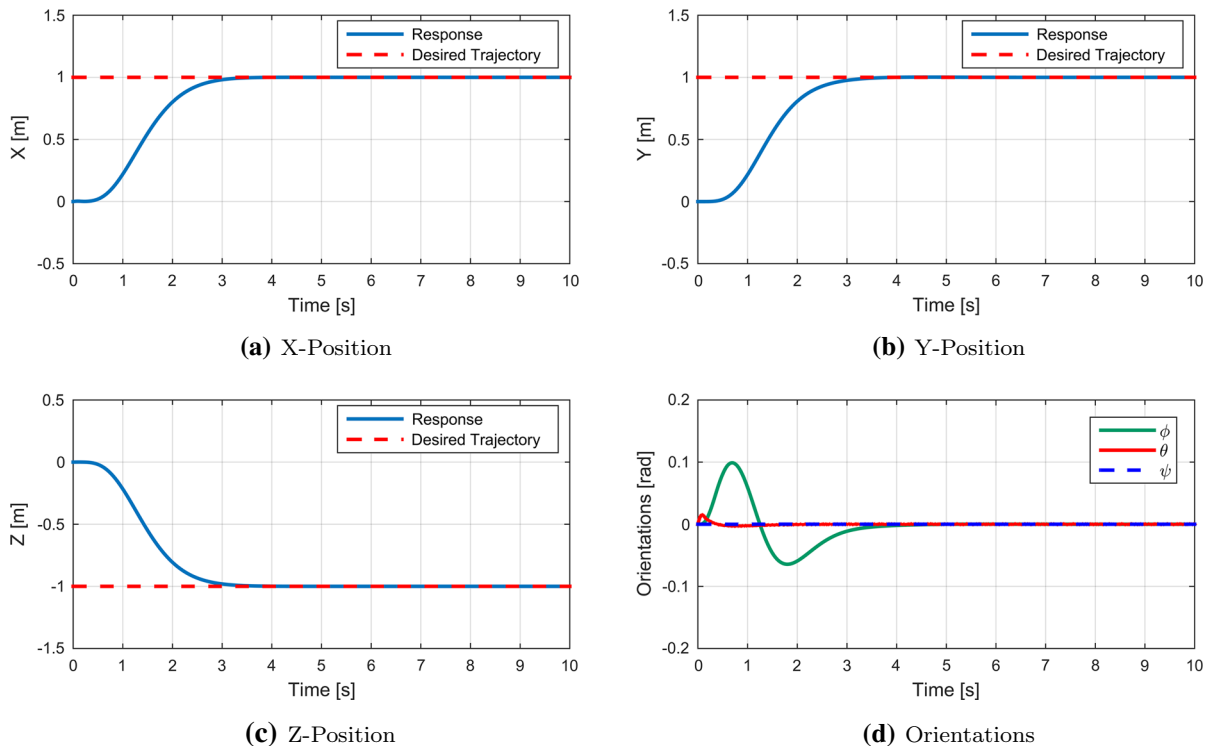


**Fig. 8** Response of the high-fidelity model's positions and orientations to step inputs

cal desired trajectory command for 20 s. The simulation shows satisfactory tracking for a varying waypoint with good precision. This validates the ability of the controller to follow dynamic reference trajectories and achieve robust performance in different simulation conditions.

In the third simulation, the FWMAV is commanded to hover in its initial position. The mass of the body is underestimated by 25% at  $t = 6$  s. A comparison between the system performance in the case of conventional SMC and ISMC is shown in Figs. 11 and 12. It highlights the role of the integral term in attaining robust performance and eliminating the external disturbance effects. Steady-state errors were eliminated, specially in the  $z$  position, where a steady-state error of 0.0209 m is found in case of conventional SMC. While in the case of ISMC the maximum tracking error at steady-state is greatly minimized to  $5.6907 \times 10^{-6}$  m.

In the fourth simulation, an external disturbance force is applied to the FWMAV in the  $x$ -direction at  $t = 6$  s with 30% of the vehicle's weight. The vehicle is commanded to hover in its initial position. As shown

in Figs. 13 and 14, the maximum steady-state error in the  $x$  position is found to be 0.0655 m in case of conventional SMC. Whereas the maximum steady-state error in case of ISMC, is  $5.4942 \times 10^{-4}$  m.

## 6 Conclusions and future work

Trajectory tracking of FWMAV is addressed in this work. A high fidelity six-DOF model which accounts for wing mass and inertia effects is developed. An aerodynamic model that includes LEV and rotational circulation effects was presented. A trajectory tracking control law was formulated, consisting of two control loops. A designed ISMC law represents the outer-loop. Unlike commonly used open-loop control allocation methods, a novel closed-loop Lyapunov-based approach utilizing aerodynamic control derivatives is developed and implemented in the inner-loop. The proposed method provides accurate continuous closed-loop solutions with less computational complexity than other iterative techniques. Simulations were carried out on averaged, time-periodic and high fidelity models.

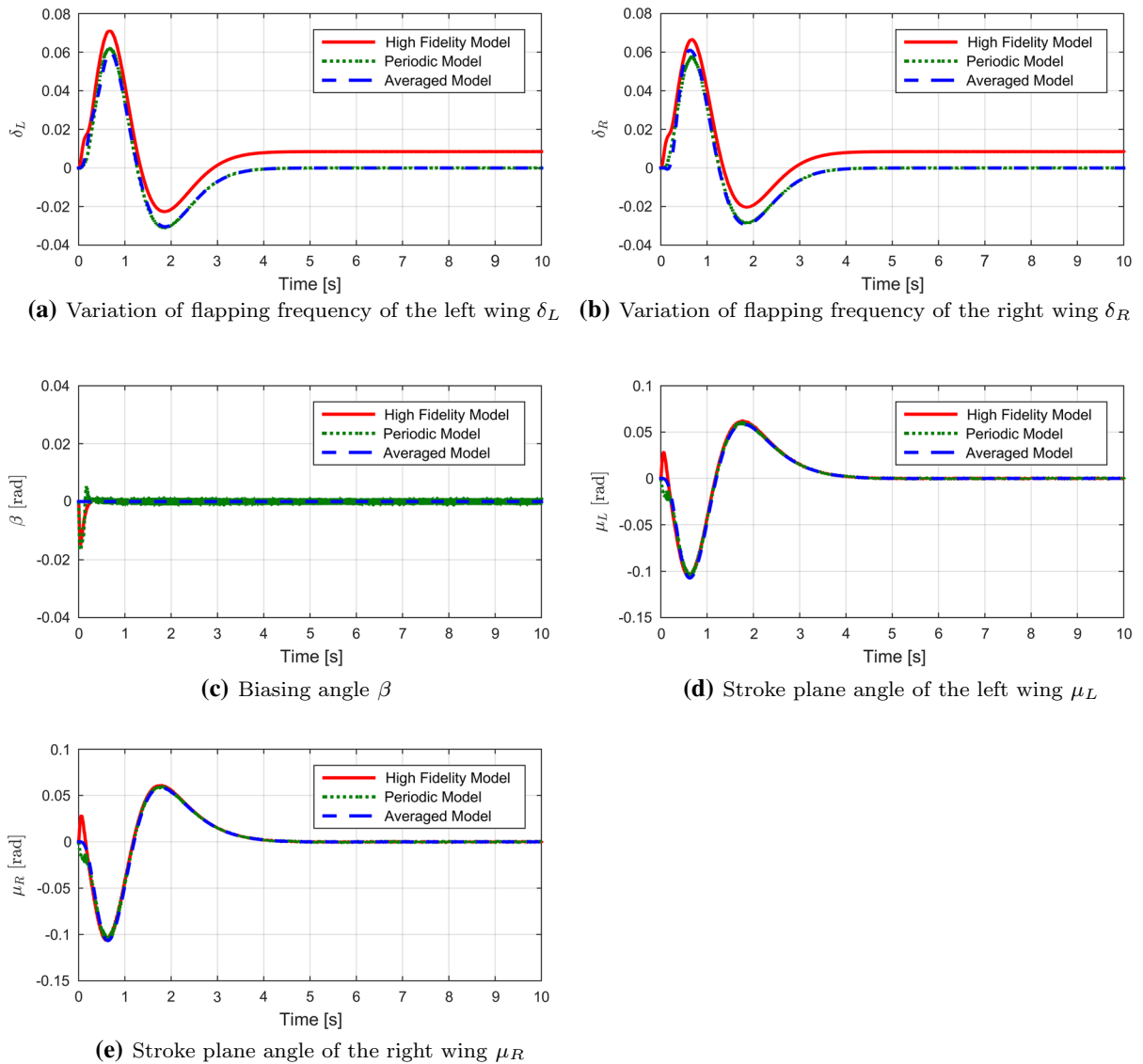


**Fig. 9** Control parameters of the FWMAV in response to a desired step inputs

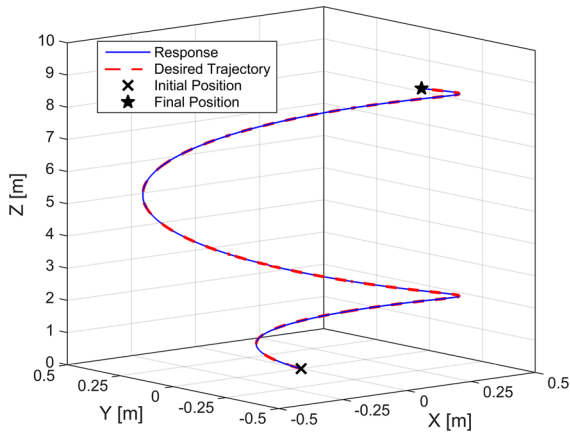


**Fig. 10** Helical trajectory

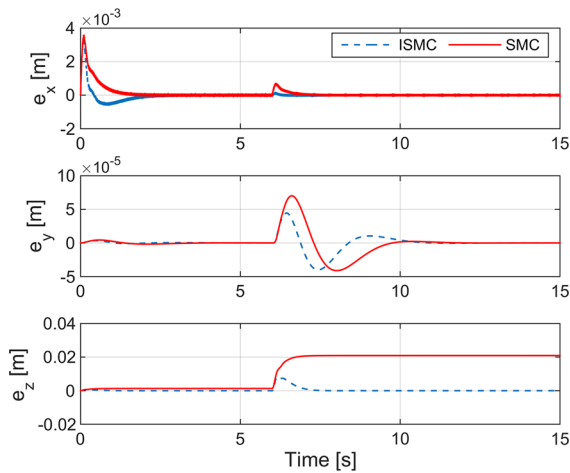


**Fig. 11** Position errors of the high-fidelity models while the mass of the body is underestimated by 25% at  $t = 6$  s

Simulation results showed that trajectory tracking was achieved successfully with feasible control effort in the existence of model uncertainties and external disturbances. Moreover, the results show rapid convergence of the errors of the command signals, obtaining smooth control parameters. Future work would include developing a dynamic model that takes into consideration wing flexibility.

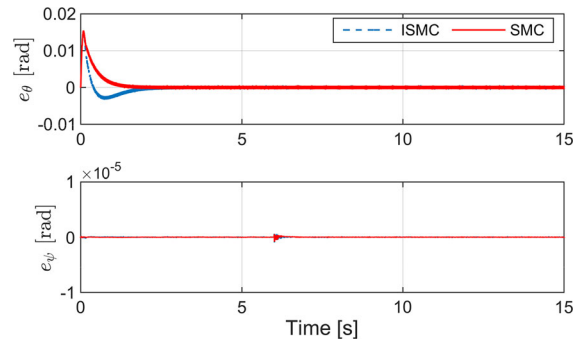


**Fig. 12** Orientation errors of the high-fidelity models while the mass of the body is underestimated by 25% at  $t = 6$  s

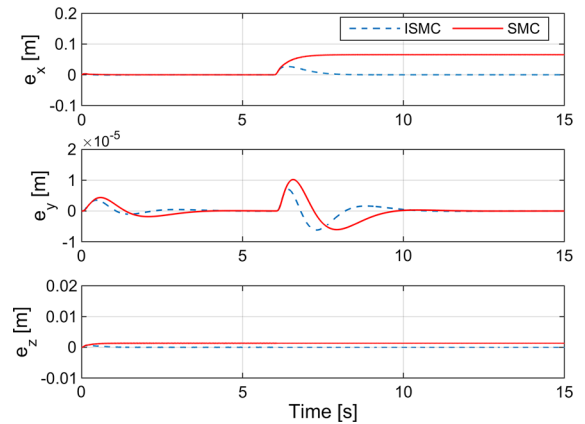


**Fig. 13** Position errors of the high-fidelity models while an external disturbance force of 30% of the vehicle's weight is applied in the  $x$ -direction at  $t = 6$  s

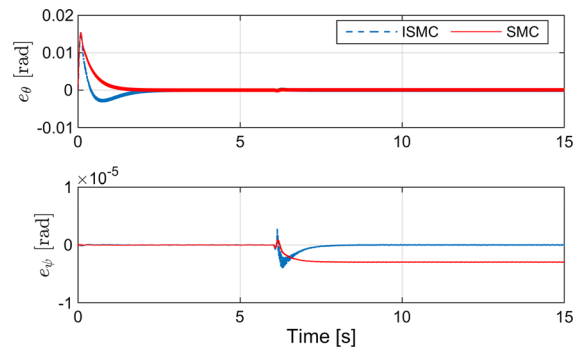


**Fig. 14** Orientation errors of the high-fidelity models while an external disturbance force of 30% of the vehicle's weight is applied in the  $x$ -direction at  $t = 6$  s

**Compliance with ethical standards**

**Conflict of interest** The authors declare that they have no conflict of interest.

**Human or animal participants** Moreover, they proclaim that the research do not involve any human or animal participants.

**Appendix A**

This appendix shows the detailed equations of control derivatives.

*X-body axis control derivatives*

$$\frac{\partial {}^b\overline{F}_{ax}}{\partial \delta_l} = -2 G_L \pi^2 \sin \mu_l (1 + \delta_l)$$

$$\frac{\partial {}^b\overline{F}_{ax}}{\partial \delta_r} = -2 G_L \pi^2 \sin \mu_r (1 + \delta_r)$$

$$\frac{\partial {}^b\overline{F}_{ax}}{\partial \beta} = 0$$

$$\frac{\partial {}^b\overline{F}_{ax}}{\partial \mu_l} = -G_L \pi^2 \cos \mu_l (1 + \delta_l)^2$$

$$\frac{\partial {}^b\overline{F}_{ax}}{\partial \mu_r} = -G_L \pi^2 \cos \mu_r (1 + \delta_r)^2$$

*Y-body axis control derivatives*

$$\frac{\partial {}^b\overline{F}_{ay}}{\partial \delta_l} = 0$$

$$\frac{\partial {}^b\overline{F}_{ay}}{\partial \delta_r} = 0$$

$$\frac{\partial {}^b\overline{F}_{ay}}{\partial \beta} = 0$$

$$\frac{\partial {}^b\overline{F}_{ay}}{\partial \mu_l} = 0$$

$$\frac{\partial {}^b\overline{F}_{ay}}{\partial \mu_r} = 0$$

*Z-body axis control derivatives*

$$\frac{\partial {}^b\overline{F}_{az}}{\partial \delta_l} = -2 G_L \pi^2 \cos \mu_l (1 + \delta_l)$$

$$\frac{\partial {}^b\overline{F}_{az}}{\partial \delta_r} = -2 G_L \pi^2 \cos \mu_r (1 + \delta_r)$$

$$\frac{\partial {}^b\overline{F}_{az}}{\partial \beta} = 0$$

$$\frac{\partial {}^b\overline{F}_{az}}{\partial \mu_l} = -G_L \pi^2 \sin \mu_l (1 + \delta_l)^2$$

$$\frac{\partial {}^b\overline{F}_{az}}{\partial \mu_r} = -G_L \pi^2 \sin \mu_r (1 + \delta_r)^2$$

*Rolling moment control derivatives*

$$\frac{\partial {}^b\overline{M}_{ax}}{\partial \delta_l} = 2 G_L \cos \mu_l (1 + \delta_l) (C_I y_{\text{cpt}} \cos \beta + \pi^2 y_H)$$

$$\frac{\partial {}^b\overline{M}_{ax}}{\partial \delta_r} = -2 G_L \cos \mu_r (1 + \delta_r) (C_I y_{\text{cpt}} \cos \beta + \pi^2 y_H)$$

$$\frac{\partial {}^b\overline{M}_{ax}}{\partial \beta} = -G_L C_I y_{\text{cpt}} \sin \beta$$

$$(\cos \mu_l (1 + \delta_l)^2 - \cos \mu_r (1 + \delta_r)^2)$$

$$\frac{\partial {}^b\overline{M}_{ax}}{\partial \mu_l} = -G_L \sin \mu_l (1 + \delta_l)^2 (C_I y_{\text{cpt}} \cos \beta + \pi^2 y_H)$$

$$\frac{\partial {}^b\overline{M}_{ax}}{\partial \mu_r} = G_L \sin \mu_r (1 + \delta_r)^2 (C_I y_{\text{cpt}} \cos \beta + \pi^2 y_H)$$

*Pitching moment control derivatives*

$$\frac{\partial {}^b\overline{M}_{ay}}{\partial \delta_l} = 2 G_L (1 + \delta_l) (C_I y_{\text{cpt}} \sin \beta + \pi^2 z_H \sin \mu_l)$$

$$\frac{\partial {}^b\overline{M}_{ay}}{\partial \delta_r} = 2 G_L (1 + \delta_r) (C_I y_{\text{cpt}} \sin \beta + \pi^2 z_H \sin \mu_r)$$

$$\frac{\partial {}^b\overline{M}_{ay}}{\partial \beta} = G_L C_I y_{\text{cpt}} \cos \beta ((1 + \delta_l)^2 + (1 + \delta_r)^2)$$

$$\frac{\partial {}^b\overline{M}_{ay}}{\partial \mu_l} = G_L \pi^2 z_H \cos \mu_l (1 + \delta_l)^2$$

$$\frac{\partial {}^b\overline{M}_{ay}}{\partial \mu_r} = G_L \pi^2 z_H \cos \mu_r (1 + \delta_r)^2$$

*Yawing moment control derivatives*

$$\frac{\partial {}^b\overline{M}_{az}}{\partial \delta_l} = -2 G_L \sin \mu_l (1 + \delta_l) (C_I y_{\text{cpt}} \cos \beta + \pi^2 y_H)$$

$$\frac{\partial {}^b\overline{M}_{az}}{\partial \delta_r} = 2 G_L \sin \mu_r (1 + \delta_r) (C_I y_{\text{cpt}} \cos \beta + \pi^2 y_H)$$

$$\frac{\partial {}^b\overline{M}_{az}}{\partial \beta} = G_L C_I y_{\text{cpt}} \sin \beta (\sin \mu_l (1 + \delta_l)^2 - \sin \mu_r (1 + \delta_r)^2)$$

$$\frac{\partial {}^b\overline{M}_{az}}{\partial \mu_l} = -G_L \cos (\mu_l) (1 + \delta_l)^2 (C_I y_{\text{cpt}} \cos \beta + \pi^2 y_H)$$

$$\frac{\partial {}^b\overline{M}_{az}}{\partial \mu_r} = G_L \cos (\mu_r) (1 + \delta_r)^2 (C_I y_{\text{cpt}} \cos \beta + \pi^2 y_H)$$

## References

- Banazadeh, A., Taymourtash, N.: Adaptive attitude and position control of an insect-like flapping wing air vehicle. *Nonlinear Dyn.* **85**(1), 47–66 (2016)
- Benamor, A., Chrifi-Alaoui, L., Ouriagli, M., Chaabane, M., Massaoud, H.: Lyapunov based second order sliding mode control for mimo nonlinear systems. *Proc. Int. J. Sci. Tech. Autom. Control IJ-STA* **5**(1), 1486–1499 (2011)
- Berman, G.J., Wang, Z.J.: Energy-minimizing kinematics in hovering insect flight. *J. Fluid Mech.* **582**, 153–168 (2007)
- Bluman, J.E., Kang, C.K., Shtessel, Y.: Control of a flapping-wing micro air vehicle: sliding-mode approach. *J. Guid. Control Dyn.* **41**(5), 1223–1226 (2018)
- Chirarattananon, P., Ma, K.Y., Wood, R.J.: Adaptive control for takeoff, hovering, and landing of a robotic fly. In: 2013 IEEE/RSJ International Conference on Intelligent Robots and Systems (IROS), pp. 3808–3815. IEEE (2013)
- Chirarattananon, P., Ma, K.Y., Wood, R.J.: Adaptive control of a millimeter-scale flapping-wing robot. *Bioinspir. Biomim.* **9**(2), 025004 (2014)
- Dickinson, M.H., Lehmann, F.O., Sane, S.P.: Wing rotation and the aerodynamic basis of insect flight. *Science* **284**(5422), 1954–1960 (1999)
- Doman, D., Oppenheimer, M., Bolender, M., Sigthorsson, D.: Altitude control of a single degree of freedom flapping wing micro air vehicle. In: AIAA Guidance, Navigation, and Control Conference, p. 6159 (2009)
- Doman, D.B., Oppenheimer, M.W., Sigthorsson, D.O.: Wingbeat shape modulation for flapping-wing micro-air-vehicle control during hover. *J. Guid. Control Dyn.* **33**(3), 724–739 (2010)
- Edwards, C., Spurgeon, S.: *Sliding Mode Control: Theory and Applications*. CRC Press, Boca Raton (1998)
- Ershkov, S.V.: A riccati-type solution of euler-poisson equations of rigid body rotation over the fixed point. *Acta Mech.* **228**(7), 2719–2723 (2017)
- Ershkov, S.V., Leshchenko, D.: On a new type of solving procedure for euler-poisson equations (rigid body rotation over the fixed point). *Acta Mech.* **230**(3), 871–883 (2019)
- Ershkov, S.V., Leshchenko, D.: On the dynamics of non-rigid asteroid rotation. *Acta Astronaut.* **161**, 40–43 (2019)
- Kalliny, A.N., El-Badawy, A.A., Elkhamisy, S.M.: Command-filtered integral backstepping control of longitudinal flapping-wing flight. *J. Guid. Control Dyn.* **41**, 1–13 (2018)
- Lee, J.S., Kim, J.K., Han, J.H.: Stroke plane control for longitudinal stabilization of hovering flapping wing air vehicles. *J. Guid. Control Dyn.* **38**(4), 800–806 (2014)
- Meirovitch, L.: *Methods of Analytical Mechanics*, p. 1354. McGraw Hill, New York (1970)
- Oppenheimer, M., Doman, D., Sigthorsson, D.: Dynamics and control of a minimally actuated biomimetic vehicle: part ii-control. In: AIAA Guidance, Navigation, and Control Conference, p. 6161 (2009)
- Oppenheimer, M., Doman, D., Sigthorsson, D.: Dynamics and control of a biomimetic vehicle using biased wingbeat forcing functions: part i-aerodynamic model. In: 48th AIAA Aerospace Sciences Meeting Including the New Horizons Forum and Aerospace Exposition, p. 1023 (2010)
- Oppenheimer, M.W., Doman, D.B., Sigthorsson, D.O.: Dynamics and control of a biomimetic vehicle using biased wingbeat forcing functions. *J. Guid. Control Dyn.* **34**(1), 204–217 (2011)
- Oppenheimer, M.W., Weintraub, I.E., Sigthorsson, D.O., Doman, D.B.: Control of a minimally actuated biomimetic vehicle using quarter-cycle wingbeat modulation. *J. Guid. Control Dyn.* **38**(7), 1187–1196 (2015)
- Serrani, A.: Robust hovering control of a single-DOF flapping wing MAV. In: American Control Conference (ACC), pp. 1302–1307. IEEE (2010)
- Slotine, J.J.E., Li, W., et al.: *Applied Nonlinear Control*, vol. 199. Prentice Hall, Englewood Cliffs (1991)
- Wood, R.J.: Design, fabrication, and analysis of a 3DOF, 3cm flapping-wing MAV. In: IEEE/RSJ International Conference on Intelligent Robots and Systems, 2007. IROS 2007, pp. 1576–1581. IEEE (2007)
- Wood, R.J.: The first takeoff of a biologically inspired at-scale robotic insect. *IEEE Trans. Rob.* **24**(2), 341–347 (2008)
- Zhang, X., Liu, H.: A three-axis pd control model for bumblebee hovering stabilization. *J. Bionic Eng.* **15**(3), 494–504 (2018)

**Publisher's Note** Springer Nature remains neutral with regard to jurisdictional claims in published maps and institutional affiliations.